JCB Journal of Cell Biology

ARTICLE

Mitochondrial-derived compartments are multilamellar domains that encase membrane cargo and cytosol

Zachary N. Wilson[1], Matt West[2], Alyssa M. English[1], Greg Odorizzi[2], and Adam L. Hughes[1]

Preserving the health of the mitochondrial network is critical to cell viability and longevity. To do so, mitochondria employ several membrane remodeling mechanisms, including the formation of mitochondrial-derived vesicles (MDVs) and compartments (MDCs) to selectively remove portions of the organelle. In contrast to well-characterized MDVs, the distinguishing features of MDC formation and composition remain unclear. Here, we used electron tomography to observe that MDCs form as large, multilamellar domains that generate concentric spherical compartments emerging from mitochondrial tubules at ER–mitochondria contact sites. Time-lapse fluorescence microscopy of MDC biogenesis revealed that mitochondrial membrane extensions repeatedly elongate, coalesce, and invaginate to form these compartments that encase multiple layers of membrane. As such, MDCs strongly sequester portions of the outer mitochondrial membrane, securing membrane cargo into a protected domain, while also enclosing cytosolic material within the MDC lumen. Collectively, our results provide a model for MDC formation and describe key features that distinguish MDCs from other previously identified mitochondrial structures and cargo-sorting domains.

Introduction

Mitochondrial architecture is continuously remodeled to support the functional demands of the organelle and to preserve homeostasis. In actively growing cells, mitochondria form a dynamic, tubular network that is separated from the cytosol by two membranes. The outer mitochondrial membrane (OMM) creates an initial barrier and establishes connections with other organelles, while the inner mitochondrial membrane (IMM) creates an impervious barrier that protects the multitude of metabolic reactions occurring in the mitochondrial matrix (Pfanner et al., 2019; Harper et al., 2020). The IMM also dynamically invaginates to form cristae, which are imperative for efficient energy production and in the establishment of several distinct aqueous and membrane subdomains within mitochondria (Iovine et al., 2021). Because of the critical role mitochondria perform in cell metabolism, several investigations have analyzed the remodeling of mitochondria that occurs to match metabolic demand (Hackenbrock, 1966; Davies et al., 2012; Kondadi et al., 2020a, 2020b). Mitochondria also reorganize their architecture in response to diverse cellular stressors, and the formation of aberrant mitochondrial structures represents a hallmark phenotype of disease states and aging (Youle and van der Bliek, 2012; Hughes and Gottschling, 2012). Indeed, the failure to prune the mitochondrial network by removing impaired or damaged portions of the organelle can actively contribute to the progression of many neurodegenerative disorders (Palikaras et al., 2018; Killackey et al., 2020). Currently, the extent of remodeling mechanisms mitochondria use to respond to different stress conditions and to preserve mitochondrial health remains incompletely understood.

Various abiotic and biotic stressors can induce mitochondrial damage, leading to the separation and degradation of whole mitochondria through a variety of selective mitophagic processes (Killackey et al., 2020; Onishi et al., 2021). Mitophagy through the PTEN-induced putative kinase 1 (PINK1)–Parkin pathway monitors mitochondrial health, in part by sensing deterioration of the mitochondrial membrane potential, which leads to the accumulation of PINK1 at the OMM. PINK1 subsequently recruits the E3 ligase Parkin, and together, these proteins initiate a phosphorylation and ubiquitylation signaling cascade that marks mitochondria for mitophagic turnover

[1]Department of Biochemistry, University of Utah School of Medicine, Salt Lake City, UT, USA; [2]Department of Molecular, Cellular, and Developmental Biology, University of Colorado Boulder, Boulder, CO, USA.

Correspondence to Adam L. Hughes: hughes@biochem.utah.edu

A.L. Hughes is the lead contact.

© 2024 Wilson et al. This article is distributed under the terms of an Attribution–Noncommercial–Share Alike–No Mirror Sites license for the first six months after the publication date (see http://www.rupress.org/terms/). After six months it is available under a Creative Commons License (Attribution–Noncommercial–Share Alike 4.0 International license, as described at https://creativecommons.org/licenses/by-nc-sa/4.0/).

Downloaded from http://rupress.org/jcb/article-pdf/223/11/e202307035/1931486/jcb_202307035.pdf by University Colorado Boulder user on 23 October 2024

(Lazarou et al., 2012; Kondapalli et al., 2012; Pickles et al., 2018). Conversely, receptor-mediated mitophagy uses distinct autophagic receptors localized on the mitochondrial surface to initiate mitophagy in response to diverse stress conditions, including starvation and hypoxia, or to remove mitochondria during development and cell differentiation (Schweers et al., 2007; Kanki and Klionsky, 2008; Esteban-Martínez et al., 2017).

Rather than reorganizing the entire mitochondrial network, some stress conditions induce mitochondria to sort cargo into distinct, membrane-bound domains leading to the piecemeal degradation of select mitochondrial cargo (Sugiura et al., 2014; Hughes et al., 2016). As a means for both steady-state turnover and in response to mild stress conditions, mitochondria form small vesicles (mitochondrial-derived vesicles, MDVs) ∼50–160 nm in diameter that form by budding away from the mitochondrial network, encapsulating cargo from just the OMM or inclusive of both mitochondrial membranes and proteins from multiple mitochondrial subdomains (Soubannier et al., 2012a, 2012b; König et al., 2021). In response to mild oxidative stress, the formation of MDVs also involves the PINK1-Parkin pathway but occurs kinetically faster than full mitophagy (McClelland et al., 2014), and in some instances can compensate for the loss of mitophagy (Towers et al., 2021), all together suggesting that MDVs may act to preserve mitochondrial health prior to removal of whole mitochondria.

Previously, in the budding yeast *Saccharomyces cerevisiae*, we identified a mitochondrial quality control pathway that also involves the selective sorting of mitochondrial proteins into a distinct domain called the mitochondrial-derived compartment (MDC). In old-aged yeast cells and in response to several acute stressors, mitochondria form large, spherical compartments that robustly sequester only a minor portion of the mitochondrial proteome (Hughes et al., 2016; Schuler et al., 2021). These MDCs are generated from a dynamic remodeling of mitochondrial membranes that rearrange at sites of contact with the ER and eventually form distinct spherical structures that contain resolvable lumens (English et al., 2020). Subsequently, MDCs are removed from mitochondria and delivered to yeast vacuoles for degradation, suggesting that MDCs act as a piecemeal autophagic mechanism that is induced to remodel or segregate select cargo from mitochondria (Hughes et al., 2016). Currently, the nature of MDC morphogenesis, the mechanisms involved in MDC formation, and the features of MDCs that distinguish them from other mitochondrial remodeling pathways all remain unresolved.

In this study, we used transmission electron microscopy (TEM) and electron tomography to determine the ultrastructural morphogenesis of MDCs. We observed that MDCs form as large, multilamellar spherical compartments that frequently encase four membrane bilayers, all of which are strongly labeled for the OMM protein Tom70. Using time-lapse fluorescence microscopy, we demonstrate that MDCs form through OMM extensions that repeatedly elongate, coalesce, and invaginate to create these compartments with layers of entrapped membrane. In doing so, MDCs engulf both OMM and cytosolic content, securing cargo into a distinct, protected domain. Collectively, these results provide a model for MDC formation and define key features that distinguish MDCs from other previously identified mitochondrial structures and cargo-sorting domains.

Results

Rapamycin treatment induces yeast to produce mitochondrial-derived multilamellar structures

Previously, we demonstrated that the inhibition of the mechanistic target of rapamycin robustly induces the formation of MDCs (Schuler et al., 2021). For example, in haploid yeast cells treated with rapamycin (Rap) for 2 h, we observe that ∼60% of cells form an MDC, demonstrated by the sequestration of the mitochondrial import receptor Tom70 into a large domain emerging from mitochondria that simultaneously excludes Tim50, an essential subunit of the Tim23 inner membrane translocase complex (Fig. 1, A and B; Hughes et al., 2016). In haploid yeast cells, MDCs typically resolve into large spherical domains, ∼400 nm in mean diameter, that contain a resolvable lumen (Fig. 1, A and C). While these aspects of MDC formation have been previously characterized (English et al., 2020), the ultrastructural morphogenesis of MDCs remains unknown.

To elucidate the structural characteristics of MDCs, we used thin-section TEM to survey the ultrastructural morphogenesis of mitochondria in the same yeast strain that was analyzed in Fig. 1, A–C. Yeast were grown to log-phase, treated with DMSO (vehicle control) or 200 nM Rap for 2 h, and then processed for TEM analyses by cryo-immobilization through high-pressure freezing followed by freeze-substituted fixation, a process that has been demonstrated to preserve membrane structure and limit fixation artifacts (West et al., 2011). In cell profiles from yeast treated with DMSO or Rap, mitochondria are readily observable as double membrane–bound organelles that form elongated tubules (longitudinal section) or small spherical organelles (cross section) with a darker luminal contrast compared with the yeast cytosol (yellow arrows, Fig. 1, D–F). Intriguingly, in cell profiles from yeast treated with Rap, we observed the formation of large (300–500 nm in diameter), spherical, multilamellar structures emerging or adjacent to mitochondrial tubules (Fig. 1, F and G). These mitochondrial-associated multilamellar structures were always observed in close proximity (within 30–50 nm) to or appeared directly attached to mitochondrial tubules. However, these structures appeared distinct from typical mitochondria because they contained multiple (>2) membrane bilayers and had a lighter luminal contrast (Fig. 1, F and G). These multilamellar structures appeared in ∼2% of cell sections surveyed (out of >800 cell profiles) near our expected frequency (∼3%) for capturing a putative MDC structure by thin-section electron microscopy. We confirmed that these structures were derived from mitochondria as they were labeled specifically with antibodies conjugated to 10-nm colloidal gold particles that targeted Tom70-GFP (Fig. 1, H–J). The labeling specificity of these antibodies is demonstrated by the frequency by which we observed gold particles at mitochondria compared with other membrane-rich organelles, such as the ER and nucleus (Fig. 1 J). Together, these results demonstrate

Downloaded from http://rupress.org/jcb/article-pdf/223/11/e202307035/1931486/jcb_202307035.pdf by University Colorado Boulder user on 23 October 2024

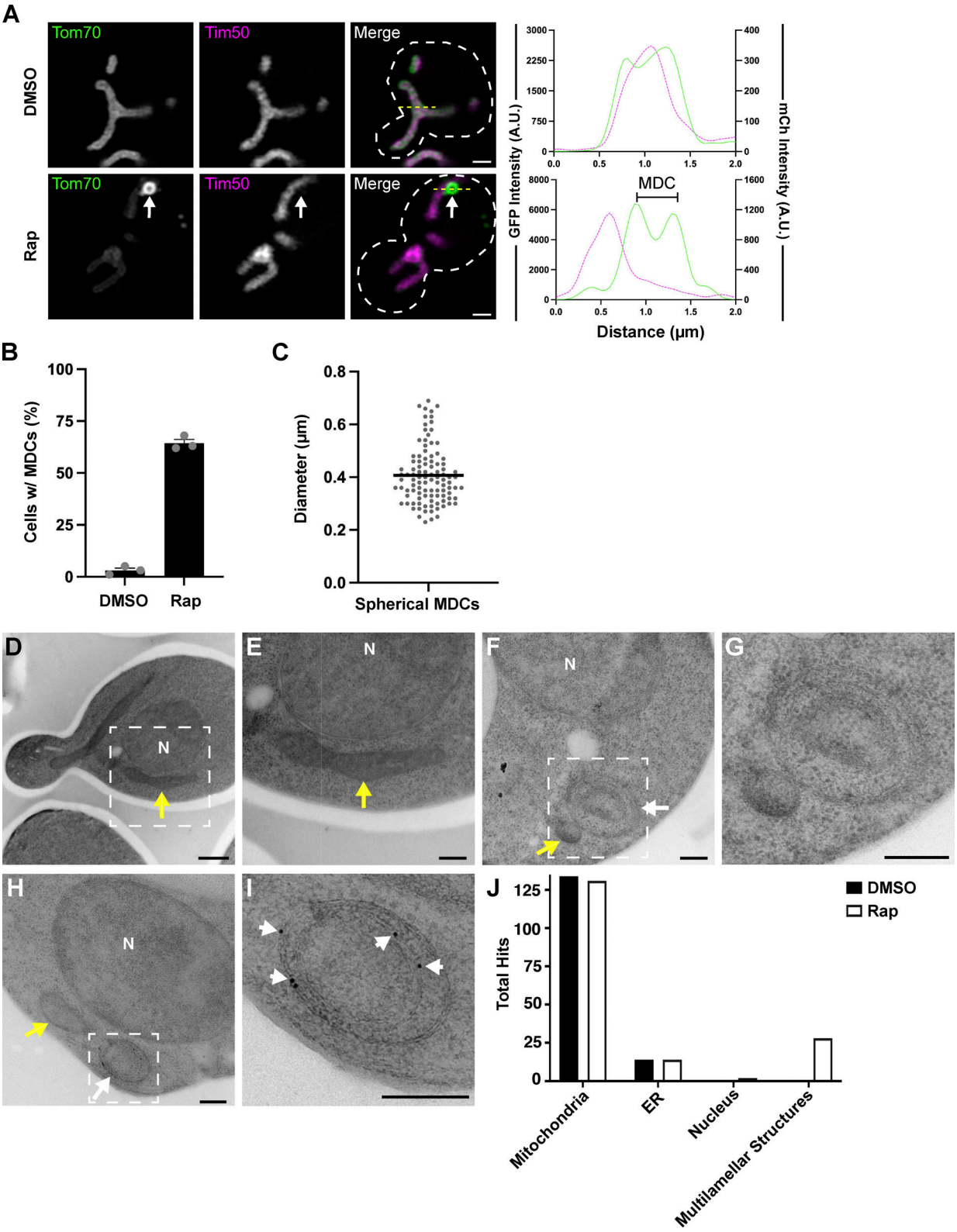

Figure 1. **Rap-treated yeast produce mitochondrial-derived multilamellar structures. (A)** Super-resolution confocal fluorescence microscopy images of DMSO or Rap-treated haploid yeast cells expressing Tom70-yEGFP and Tim50-mCherry. MDCs are indicated by white arrows. Scale bar = 1 µm. Yellow line marks the position of the line-scan fluorescence intensity profile shown on the right. The left and right y axes correspond to Tom70-GFP and Tim50-mCherry fluorescence intensity, respectively. The bracket denotes MDC. **(B)** Quantification of MDC formation in DMSO or Rap-treated yeast. Error bars show mean ± SE of three replicates, $n \geq 100$ cells per replicate. **(C)** Scatter plot showing the diameter of Rap-induced MDCs. The black line indicates the mean (0.41 µm) of $n = 104$ MDCs. **(D–I)** Thin-section TEM analysis of 80-nm cell sections from the same yeast strain analyzed above. Yeast were treated with either DMSO (D and E) or 200 nM Rap (F–I). White dotted-line squares in D, F, and H indicate the region magnified and shown in E, G, and I, respectively. Yellow arrows: mitochondria,

Downloaded from http://rupress.org/jcb/article-pdf/223/11/e202307035/1931486/jcb_202307035.pdf by University Colorado Boulder user on 23 October 2024

white arrows: multilamellar structures, N: Nucleus. Scale bars = (D) 500 nm (E–I) 200 nm. **(H and I)** Immunogold labeling with monoclonal antibodies targeting GFP and secondary antibodies conjugated to 10-nm gold particles. White arrowheads in I point to gold particles. **(J)** Quantification of the total anti-GFP immunogold particles that labeled the indicated cell structures from an analysis of >100 cell sections.

that Rap treatment induces yeast to produce mitochondrial-derived multilamellar structures.

Initially, we characterized the formation of MDCs in aged yeast cells and in yeast treated with the Vacuolar H^+-ATPase inhibitor, Concanamycin A (ConcA), which mimics the alkalinization of vacuoles that occur during yeast aging (Hughes et al., 2016; Hughes and Gottschling, 2012). While treating cells with 500 nM ConcA induces MDC formation, MDCs are less frequent (forming in ∼40% of cells) and resolve into spherical domains that are slightly smaller (∼360 nm in mean diameter) than those produced after Rap treatment (Fig. S1, A–C; Schuler et al., 2021). Even though MDCs form less frequently after ConcA treatment, we still observed the formation of mitochondrial-associated multilamellar structures in cell profiles derived from yeast that had been treated with 500 nM ConcA for 2 h (Fig. S1 D). These multilamellar structures were also mitochondrial derived as immunolabeling demonstrated that they contained Tom70-GFP (Fig. S1, D and E). Considering the mitochondrial network is preserved in Rap-treated cells and that MDCs form more frequently upon Rap treatment, we focused the rest of our EM analyses on yeast treated with Rap.

Mitochondrial-derived multilamellar structures enrich for Tom70-GFP and exclude Tim50-mCherry

A defining feature of MDCs is the exclusion of most mitochondrial proteins, including the inner membrane protein Tim50 (Fig. 1 A). Notably, a dual-labeled immunoelectron analysis demonstrated that while the Rap-induced mitochondrial-derived multilamellar structures labeled strongly for Tom70-GFP, they were largely devoid of Tim50-mCherry (Fig. 2). A serial-section reconstruction derived from thin-section TEM images of a dual immuno-labeled multilamellar structure revealed that this structure formed an elongated, spherical compartment that appeared to be enclosing at two tapered ends (Fig. 2, A–E; and Video 1). Other than the two tapered ends, this structure appeared completely enclosed. However, we cannot exclude the possibility that small (∼10–30 nm) openings exist, and we did not capture the entirety of this mitochondrial-derived multilamellar structure (Fig. 2, A–E; and Video 1). The outer compartment was ∼520 nm in diameter and was bound by two closely apposed membrane bilayers that surrounded a second compartment (∼490 nm in diameter) also formed by two closely apposed membrane bilayers (Fig. 2, A–C; and Video 1). Additionally, this mitochondrial-derived multilamellar structure appeared to be directly adjacent to a mitochondria–ER contact site, as the ER was identified based on the size and contrast staining that were consistent with prior observations for ER membranes (Fig. 2, D and E, ER is colored in yellow; and Video 1; West et al., 2011), and near an additional double-membrane vesicular structure that labeled strongly for Tom70-GFP (Fig. 2 E, top left and labeled in green; and Video 1).

Antibodies conjugated to 6-nm colloidal gold particles that targeted Tom70-GFP could be observed throughout the reconstructed multilamellar structure, including within the interior (cyan-labeled dots), between and on both sets of double membrane compartments (cyan-labeled dots), and externally on the surface of the larger compartment (green-labeled dots) (Fig. 2, A and C–E; and Video 1). Conversely, antibodies conjugated to 10-nm colloidal gold particles that targeted Tim50-mCherry were only observed along mitochondrial tubules and unenriched within the adjacent multilamellar compartment (Fig. 2, B–E; and Video 1). A larger dual-labeled immunoelectron analysis of 178 cell profiles revealed that antibodies detecting Tim50-mCherry are consistently absent from these mitochondrial-derived multilamellar structures (Fig. 2 F). The absence of Tim50-mCherry within these domains cannot be attributed simply to the lower protein abundance of Tim50 compared to Tom70, as antibodies against either protein strongly labeled mitochondria but Tim50 was more depleted in the multilamellar structures compared to the reduction in labeling observed at mitochondria (Fig. 2 F).

Mitochondrial-derived multilamellar structures contain sets of paired membrane bilayers

Prompted by our observations from thin-section TEM, we examined the ultrastructure of mitochondria after Rap treatment by thick-section electron tomography. Electron tomography from yeast treated with Rap for 2 h revealed the formation of spherical, multilamellar structures (labeled green) that were bound by two (Fig. 3, A–C; and Video 2) or four membrane bilayers (Fig. 3, D–I; and Videos 3 and 4) in contact with mitochondrial tubules. All of these structures contained a lighter luminal contrast staining distinct from the contrast staining observed in the adjacent mitochondrial tubules and comparable with the surrounding cytosol (Fig. 3 and Videos 2, 3, and 4). Measuring from the limiting membrane, the smaller double-membrane structures were ∼135 and ∼170 nm in diameter (Fig. 3, A–C), while the larger, multilamellar structures were bound by a set of two closely apposed membrane bilayers (∼420 nm in diameter, Fig. 3, D–F; ∼270 nm in diameter, Fig. 3, G–I) that surrounded an internal layer of closely apposed paired membranes (∼370 nm in diameter, Fig. 3, D–F; ∼210 nm in diameter Fig. 3, G–I). The diameters of these larger, multilamellar structures are consistent with our measurements of MDC diameter from super-resolution fluorescence microscopy (Fig. 1 C). Noticeably, each of these multilamellar structures were near an ER–mitochondria contact site or directly in contact with the ER, which was identifiable based on the continuity of the ER membranes that also contained areas with bound ribosomes (Figs. 2 and 3; and Videos 1, 2, 3, and 4; ER labeled in yellow). These observations are consistent with results from a prior investigation that showed that MDCs form at ER–mitochondria contact sites and also require ER–mitochondria contact sites for MDC biogenesis (English et al., 2020). Interestingly,

Downloaded from http://rupress.org/jcb/article-pdf/223/11/e202307035/1931486/jcb_202307035.pdf by University Colorado Boulder user on 23 October 2024

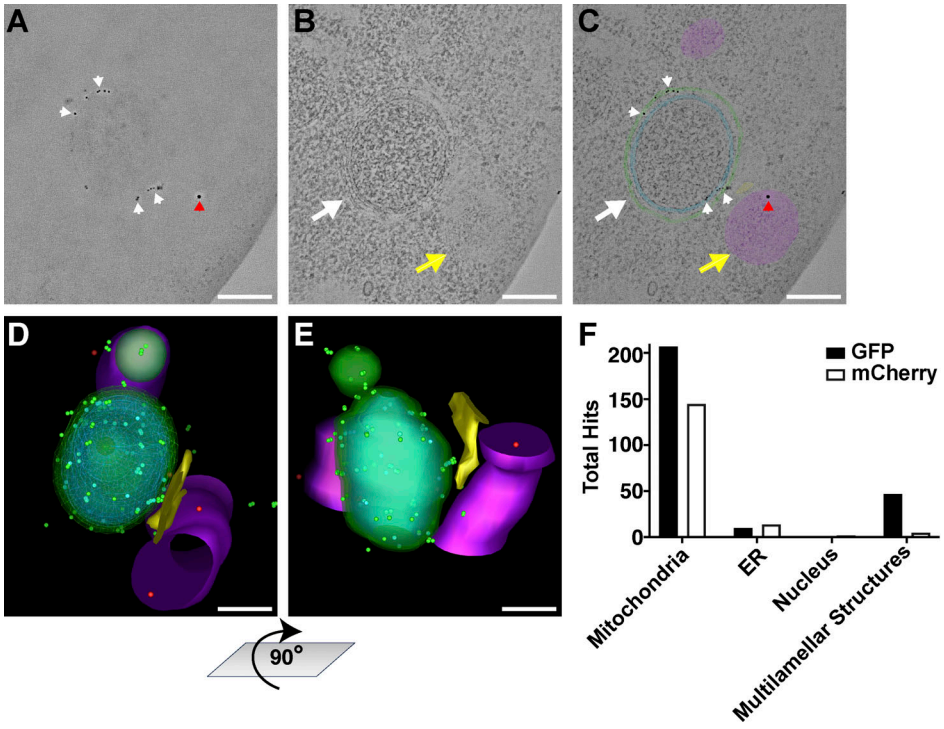

Figure 2. **Mitochondrial-derived multilamellar structures are enriched for Tom70-GFP and exclude Tim50-mCherry. (A–E)** Dual-immuno tomography obtained from five 90-nm cell sections of a yeast cell expressing Tom70-yEGFP and Tim50-mCherry treated with 200 nM Rap. Secondary antibodies conjugated to 6-nm or 10-nm gold particles targeted primary antibodies for GFP or mCherry, respectively. Scale bar = 200 nm. See related Video 1. **(A)** Tomograph of the immune-reactive surface of the middle section (cell section #3). White arrowheads point to 6-nm gold particles, red arrowheads point to 10-nm gold particles. **(B)** Tomograph of the mid-plane of the middle section (cell section #3). Yellow arrow: mitochondria, white arrow: multilamellar structure. **(C)** Model overlay of section 3. Purple labels mitochondria, green labels the outer layer of doublet membranes, while cyan labels the internal layer of doublet membranes in the mitochondrial-derived multilamellar structure. **(D)** 3D model of the dual-immuno tomography described above. The mitochondrial-derived multilamellar structure is wire-modeled with the limiting membrane of the outer double-membrane labeled in green and the inner doublet membrane labeled in cyan. 6-nm gold particles appearing on the outer surface are overlayed with green spheres, while 6-nm gold particles appearing within the multilamellar structure are overlayed with cyan spheres. 10-nm gold particles are overlayed with red spheres. Mitochondria: purple, ER: yellow. **(E)** Same 3D model as shown in D rotated vertically 90°. **(F)** Quantification of the total anti-GFP 6-nm and anti-mCherry 10-nm immunogold conjugated secondary antibodies that labeled the indicated cell structures from a thin-section TEM analysis of 178 cell sections from yeast expressing Tom70-yEGFP and Tim50-mCherry that were treated with 200 nM Rap.

another serial-section reconstruction of a large (~720 nm in diameter) multilamellar structure that robustly labeled with antibodies targeting Tom70-GFP showed extensive ER contact, potentially indicating that ER contact with MDCs increases as these structures grow in size (Fig. S2, A–C; and Video 7). For consistency most of our electron microscopy analyses were performed on the same yeast strain that was analyzed in Fig. 1; however, we also observed by electron tomography similar large, spherical, multilamellar structures adjacent to mitochondria and ER–mitochondria contact sites in the wild-type BY4741 strain treated with Rap (Fig. 3, G–I; and Video 4), supporting previous observations that MDC formation is not driven by the presence of fluorescent proteins (Schuler et al., 2021). In total, the results from our electron microscopy analyses support the interpretation that MDCs are formed from multiple layers of mitochondrial membrane and contain luminal content distinct from the mitochondrial matrix.

While autophagosomes frequently associate with mitochondria, and it has been reported that mitochondrial membranes and ER–mitochondria contact sites support autophagosome biogenesis (Hailey et al., 2010; Hamasaki et al., 2013), we considered it unlikely that autophagosomal membranes were involved in generating MDCs. Previously, we demonstrated that both the core autophagy machinery and the yeast mitophagy receptor Atg32 are not required for MDC formation (Hughes et al., 2016). Furthermore, when we analyzed the localization of Rap-induced GFP-Atg8 foci compared with MDCs to assess if MDCs are bound by autophagosomal membranes, we observed that GFP-Atg8 foci did not colocalize with MDCs and were only within close proximity to MDCs about 15% of the time (orange arrows, Fig. S2, D and E). We also frequently observed MDCs near the cell periphery, while autophagosomes form and are often observed in close proximity to the vacuole (Fig. S2, F–I; Suzuki et al., 2013), and by electron tomography, autophagosomes often contained internal vesicles, which we have yet to see inside MDCs and we have not observed other organelles inside MDCs (Fig. S2, F–I, autophagosome labeled in orange). Moreover, our immunolabeling experiments for Tom70-GFP demonstrated that Tom70-GFP is found at both the surface and within internal membranes of MDCs, altogether indicating that MDCs are not additionally bound by autophagosomal membranes.

Downloaded from http://rupress.org/jcb/article-pdf/223/11/e202307035/1931486/jcb_202307035.pdf by University Colorado Boulder user on 23 October 2024

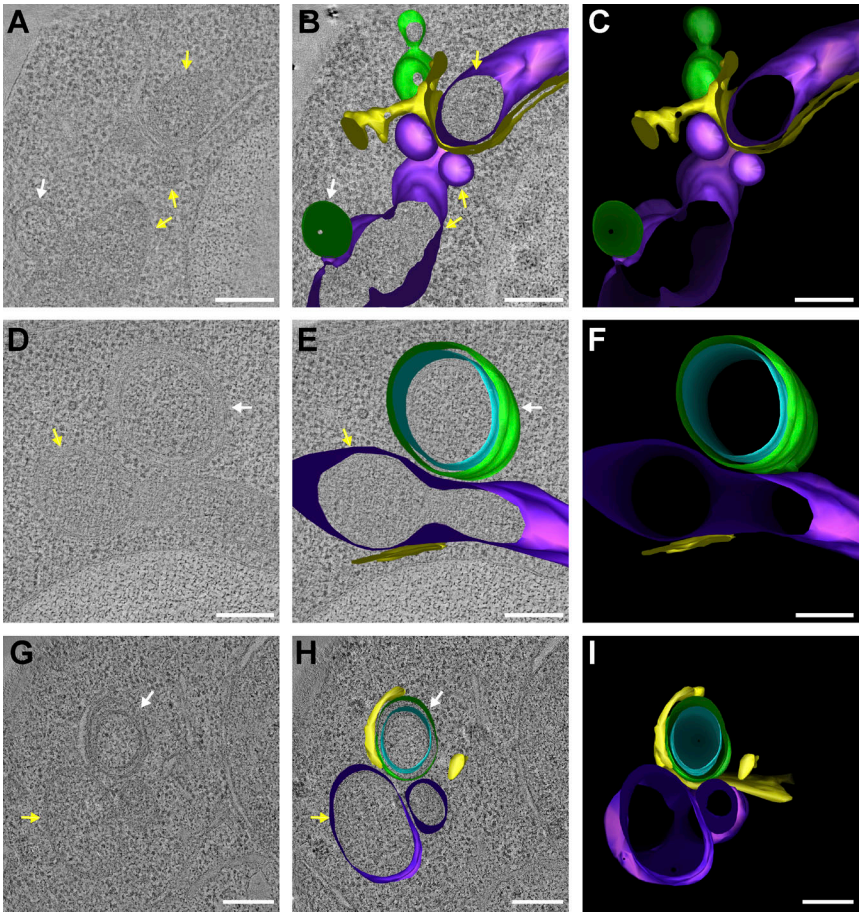

Figure 3. **Mitochondrial-derived compartments contain sets of paired membranes. (A–I)** 2D cross sections and 3D models derived from 200-nm cell sections of yeast cells treated with 200 nM Rap. Scale bar = 200 nm. See associated Videos 2, 3, and 4. **(A)** Tomograph of a small, putative MDC bound by a single double-membrane from a haploid yeast cell expressing Tom70-yEGFP and Tim50-mCherry treated with 200 nM Rap. Yellow arrows: mitochondria, white arrow: MDC. **(B)** Model overlay of the tomograph shown in A. **(C)** 3D model of small, putative MDCs bound by a single double-membrane (labeled green). Mitochondria: purple, ER: yellow. See associated Video 2. **(D)** Tomograph of a larger, putative MDC bound by four membrane bilayers from a haploid yeast cell expressing Tom70-yEGFP and Tim50-mCherry treated with 200 nM Rap. Yellow arrow: mitochondria, white arrow: MDC. **(E)** Model overlay of the tomograph shown in D. **(F)** 3D model of the larger, putative MDC bound by two closely apposed paired membranes. The limiting membrane of the outer doublet membrane is labeled green, while the internal doublet membrane is labeled cyan. Mitochondria: purple, ER: yellow. See associated Video 3. **(G)** Tomograph of a larger, putative MDC bound by four membrane bilayers from the wild-type BY4741 yeast strain. Yellow arrow: mitochondria, white arrow: MDC. **(H)** Model overlay of the tomograph shown in D. **(I)** 3D model of the larger, putative MDC bound by two closely apposed paired membranes. The limiting membrane of the outer doublet membrane is labeled green, while the internal doublet membrane is labeled cyan. Mitochondria: purple, ER: yellow. See associated Video 4.

MDCs form through membrane extension intermediates

To investigate how mitochondria rearrange to form MDCs and capture the layers of membrane we observed in our ultrastructural analyses, we followed MDC biogenesis using time-lapse imaging of live yeast cells by fluorescence microscopy. Yeast expressing Tom70-GFP alone or Tom70-GFP and Tim50-mCherry were imaged every minute over a 2-h time course after MDC formation was induced via treatment with 200 nM Rap. Often within the first 20 min, we observed a membrane extension containing only Tom70-GFP that would extend along or emerge from mitochondria and subsequently fold back on itself to create a bright, spherical focus enriched for Tom70-GFP (Fig. 4, A–C; and Video 5 and Video 6). Through seven separate experiments that captured 52 Rap-induced MDC biogenesis events, we observed that 43 of the MDC forming events (~83%) began through a membrane extension intermediate that subsequently coalesced into a Tom70-GFP focus with greater fluorescence intensity than Tom70-GFP on the mitochondrial tubule (Fig. 4 B). Sometimes these bright Tom70-GFP foci would grow into large spherical domains with resolvable lumens that we have been defining as MDCs. However, frequently we found that the Tom70-GFP foci would repeat the process described above, continuing to grow and extend, creating bright, elongated extensions that invaginated prior to resolving into a large spherical compartment with a resolvable lumen (Fig. 4 C; Video 6; Fig. S3 A; and Video 8). Importantly, we also observed that MDCs generated in response to other stressors, such as ConcA or cycloheximide (CHX) treatment, also formed through a membrane extension intermediate that subsequently coalesced into a bright Tom70-GFP focus (Fig. S3, B–E; and Videos 9 and 10). Frequently, these bright Tom70-GFP foci would also continue to grow, extend, and invaginate inward prior to resolving into large spherical compartments (Fig. S3, B and D; and Videos 9 and 10), suggesting this is a common mechanism of MDC biogenesis. In total, these examples of Tom70-GFP–positive membranes that appear to repeatedly extend and fold inward provide an explanation for how MDCs contain layers of membrane as observed by our ultrastructural analyses.

Because our time-lapse imaging demonstrated that MDCs form through dynamic rearrangements of mitochondrial membranes that frequently but not always resolve into large spherical compartments, we quantitatively assessed the structural diversity of MDCs at the 2-h time point after Rap treatment. We binned the MDC morphologies that we observed into four categories: large spherical compartments with a resolvable lumen (compartment, Comp), bright spherical foci without a resolvable lumen (large spheres, LS), bright membrane extensions (BME), or MDCs that formed as amorphous structures we defined as irregular-shaped Tom70-GFP–enriched clusters (ISC) (Fig. 4 D). From this quantitative analysis, we observed that most MDCs resolved into large spherical domains with (~33%) or without (~28%) resolvable lumens, consistent with our prior definition

Downloaded from http://rupress.org/jcb/article-pdf/223/11/e202307035/1931486/jcb_202307035.pdf by University Colorado Boulder user on 23 October 2024

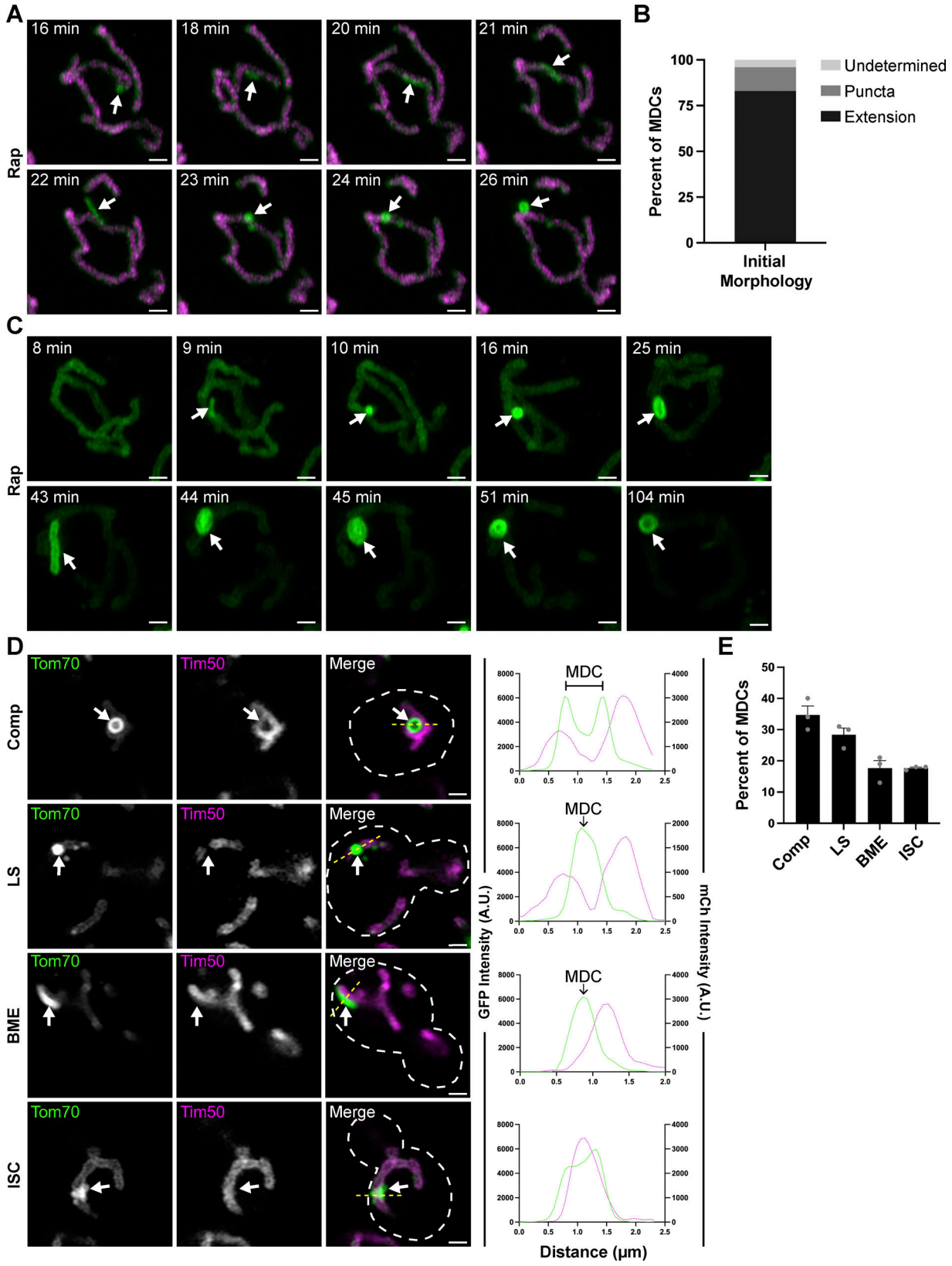

Figure 4. **MDCs form through membrane extension intermediates. (A)** Super-resolution time-lapse images of Rap-induced MDC formation in yeast cells expressing Tom70-yEGFP and Tim50-mCherry. Images were acquired over 120 min. White arrows mark MDC. Scale bar = 1 µm. See associated Video 5. **(B)** Quantification of the initial morphology of Tom70-yEGFP structures during MDC biogenesis. *n* = 52 events from seven experiments. **(C)** Super-resolution time-lapse images of Rap-induced MDC formation in yeast cells expressing Tom70-yEGFP. Images were acquired over 120 min. White arrows mark MDC. Scale bar = 1 µm. See associated Video 6. **(D)** Representative super-resolution confocal fluorescence microscopy images of diverse MDC morphologies

Downloaded from http://rupress.org/jcb/article-pdf/223/11/e202307035/1931486/jcb_202307035.pdf by University Colorado Boulder user on 23 October 2024

observed in Rap-treated haploid yeast expressing Tom70-yEGFP and Tim50-mCherry. MDC structures are indicated by white arrows. Scale bar = 1 µm. The yellow line marks the position of the line-scan fluorescence intensity profile shown to the right. The left and right y axes correspond to Tom70-yEGFP and Tim50-mCherry fluorescence intensity, respectively. Comp = compartment, LS = large spheres, BME = bright membrane extensions, ISC = irregular-shaped clusters. **(E)** Quantification of the MDC morphologies shown in D as a percent of total MDCs. Error bars show mean ± SE of three replicates, $n > 60$ MDCs per replicate.

of MDCs (Fig. 4 E; Hughes et al., 2016; English et al., 2020). However, the final third of MDC structures were evenly split between BME and ISC morphologies, demonstrating that either MDCs continue to form over a long time period or that they do not always form clear compartment-like structures (Fig. 4 E). In support, we occasionally observed multiple MDCs forming in one cell (Fig. S3 A and Video 8) and also captured multiple MDCs with diverse morphologies all within one cell (Fig. S3 F). While rare, we also observed MDCs with clear, resolvable, internal membrane invaginations (Fig. S3 G). These observations further supported our results that MDCs encapsulate layers of membrane and demonstrated that these features of MDCs can be observed in a steady-state analysis of MDC morphology.

Tom70-GFP-IAA7 is protected within MDCs from the auxin-degron system

Our time-lapse imaging experiments support our ultrastructural analyses that MDCs form as multilamellar compartments through repeated engulfment of the OMM. These results suggest that outer membrane proteins enclosed within the limiting membrane of MDCs should be protected from cytosolic degradation machinery. To assess this hypothesis experimentally, we fused an auxin-inducible degron to the C-terminus of Tom70-GFP (Tom70-GFP-IAA7; Nishimura et al., 2009). In cells treated with 1 mM indole-3-acetic acid (auxin), Tom70-GFP-IAA7 was rapidly degraded within the first 30 min (Fig. 5 A). While Tom70-GFP-IAA7 was rapidly degraded after auxin treatment, auxin had no detectable effect on the protein levels of several mitochondrial proteins, including the Tom70 paralog, Tom71, demonstrating that the auxin-induced degradation of Tom70-GFP-IAA7 is selective (Fig. 5 A). In diploid yeast cells expressing Tom70-GFP-IAA7 from one endogenous locus and Tom70-mCherry from the other locus, auxin treatment led to the near complete depletion of Tom70-GFP-IAA7 throughout the entire mitochondrial network while Tom70-mCherry remained unaffected (Fig. 5 B). Rap treatment led to robust sequestration of both Tom70-GFP-IAA7 and Tom70-mCherry into MDCs (Fig. 5 C, top panels), demonstrating that the auxin-inducible degron did not alter the recruitment of Tom70-GFP into MDCs. Intriguingly, when we treated with Rap for 2 h to establish MDCs and then added auxin, we observed a nearly complete depletion of Tom70-GFP-IAA7 throughout the mitochondrial tubule (Fig. 5 C, yellow arrows in Rap + Aux panels), while Tom70-GFP-IAA7 remained protected within MDCs (Fig. 5 C, white arrows in Rap + Aux panels). The protection of Tom70-GFP-IAA7 could also be observed in whole-cell lysates analyzed via western blot as Tom70-GFP-IAA7 was degraded at a slower rate in cells treated with Rap prior to auxin treatment compared with those treated with a vehicle control prior to auxin treatment (Fig. 5 D). Note that the strong reduction of Tom70-GFP-IAA7 levels at the 0 h time point in Rap-treated cells are due, in part, to a block in protein synthesis induced by Rap treatment.

To further analyze the impact of MDC sequestration on the auxin-induced degradation of Tom70-GFP-IAA7, we performed a time-course experiment, capturing the fluorescence intensities of Tom70-GFP-IAA7 and Tom70-mCherry in cells that were either preinduced or uninduced for MDC formation 2 h prior to treatment with either auxin or a vehicle control. Upon auxin or vehicle treatment, we captured live-cell images on large cell populations ($n > 100$ cells) every 45 min for 3 h. A plot providing the ratio of the mean fluorescence intensity of Tom70-GFP-IAA7 found within the mitochondrial tubule after auxin treatment compared to the vehicle control demonstrates the rapid and near complete removal of Tom70-GFP-IAA7 by the 45 min time point, which then remained nearly undetectable throughout the rest of the three-hour time-course experiment (Fig. 5 E). In comparison, the levels of Tom70-mCherry remained unaffected by auxin treatment highlighted by a fluorescence intensity ratio that consistently hovered around one (Fig. 5 E). In contrast to the rapid auxin-induced degradation of Tom70-GFP-IAA7 in mitochondrial tubules, Tom70-GFP-IAA7 sequestered in MDCs was protected from auxin-induced degradation, illustrated by the slower depletion of Tom70-GFP-IAA7 fluorescence intensity within MDCs (Fig. 5 F). By the end of the 3-h time course, the amount of Tom70-GFP-IAA7 observed within MDCs had diminished to a quarter of its initial fluorescence intensity but never dropped to the nearly undetectable levels caused by auxin-induced degradation within mitochondrial tubules (Fig. 5 F). While these results demonstrate that Tom70-GFP-IAA7 is protected within MDCs, they also suggest that a significant portion of Tom70-GFP-IAA7 can still be degraded within MDCs. As support, using super-resolution fluorescence microscopy, we occasionally observed that Tom70-GFP-IAA7 was more protected within the interior compartment of MDCs compared with the outer membranes of the MDC (Fig. S4 A).

The MDC lumen contains cytosolic material

Next, we wanted to determine the nature of the material within the MDC lumen. Based on the appearance of the MDC lumen in our electron micrographs, we hypothesized that cytosol is engulfed within the MDC interior. We began by testing if cytosolic material is excluded from MDCs as it is from mitochondria. To do so, we expressed GFP in cells also expressing Tom70-mCherry and induced MDC formation with Rap treatment. In these cells, GFP filled the entire cytosol and nucleoplasm but was clearly excluded from the interior of yeast vacuoles and mitochondrial tubules (Fig. 6 A, yellow arrows). In contrast, we could distinguish neither an exclusion of cytosolic GFP from MDCs nor an enrichment of cytosolic GFP within MDCs (Fig. 6 A, white arrows). Similarly, we did not observe the exclusion of cytosolic GFP from MDCs induced by other stress conditions

Downloaded from http://rupress.org/jcb/article-pdf/223/11/e202307035/1931486/jcb_202307035.pdf by University Colorado Boulder user on 23 October 2024

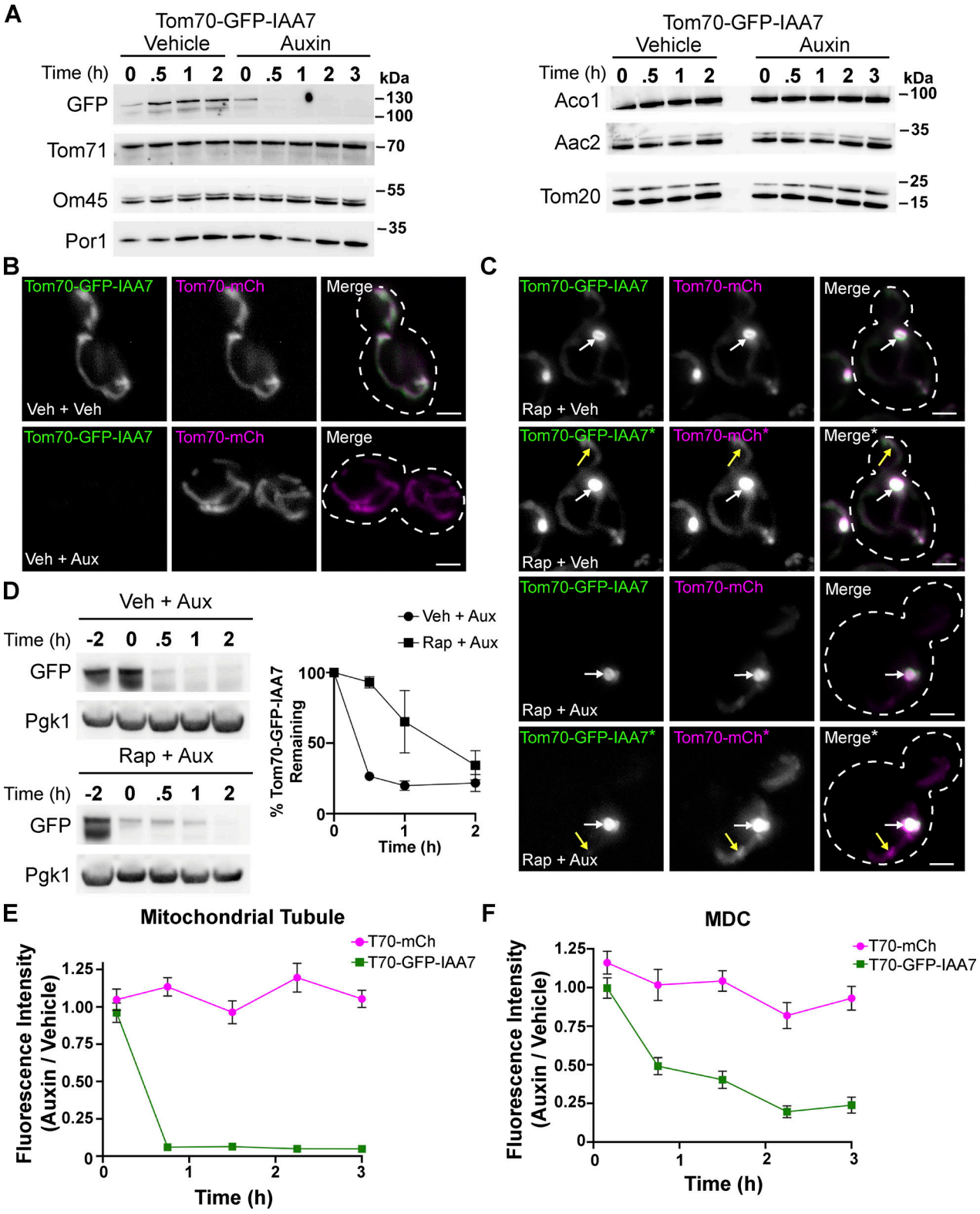

Figure 5. **Tom70-GFP-IAA7 is protected within MDCs from the auxin-degron system. (A)** Immunoblots of whole-cell protein extracts from yeast expressing Tom70-yEGFP-IAA7 and probed for the indicated mitochondrial proteins or GFP. Extracts were obtained at the indicated time points after treatment with either 1 mM auxin or an equivalent volume of 70% ethanol (vehicle). **(B)** Max projections of widefield fluorescence microscopy images of yeast cells expressing Tom70-GFP-IAA7 and Tom70-mCherry. Images were taken 1.5 h after treatment with either 1 mM auxin (Veh + Aux) or an equivalent volume of 70% ethanol (Veh + Veh), which were both added 2 h after treatment with DMSO. Scale bar = 2 µm. **(C)** Similar analysis as shown in B except yeast cells were treated with 200 nM Rap 2 h prior to treatment with either auxin (Rap + Aux) or an equivalent volume of 70% ethanol (Rap + Veh). Yellow arrows indicate mitochondrial tubule, white arrows indicate MDCs. *Panels showing an increased pixel intensity. Scale bar = 2 µm. **(D)** Immunoblot of whole-cell protein

Downloaded from http://rupress.org/jcb/article-pdf/223/11/e202307035/1931486/jcb_202307035.pdf by University Colorado Boulder user on 23 October 2024

extracts from yeast expressing Tom70-GFP-IAA7. Extracts were obtained at the indicated time points around treatment with 1 mM auxin. Auxin treatment occurred 2 h after treatment with either 200 nM Rap or DMSO (Vehicle) and a whole-cell protein extract sample was obtained prior to drug treatment (−2). Pgk1 is provided as a loading control. The graph on the right shows the quantification of the percent Tom70-GFP-IAA7 remaining after auxin treatment normalized to the Pgk1 loading control; error bars show mean ± SD of three independent experiments. **(E)** An analysis comparing the fluorescence intensities elicited by either Tom70-mCherry or Tom70-GFP-IAA7 within the mitochondrial tubule at the indicated time points. Fluorescence intensity is shown as a ratio of emissions from mitochondrial tubules of auxin-treated cells/vehicle-treated cells. **(F)** A similar analysis as shown in E except the fluorescence intensity ratios were derived from comparing emissions from MDCs of auxin-treated cells/vehicle-treated cells. Source data are available for this figure: SourceData F5.

(Fig. S4 B), demonstrating that MDCs, in general, can be infiltrated with cytosolic material. Furthermore, as a comparison, we used an auxin-induced degron system to acutely dissolve the ER–mitochondria encounter structure (ERMES), which resulted in the appearance of swollen mitochondrial tubules and spheres as previously reported (John Peter et al., 2022). Even though mitochondrial architecture was lost in these cells, cytosolic GFP was still strongly excluded from the lumen of these aberrant mitochondria (Fig. 6 B, yellow arrows). Altogether, these results are consistent with our TEM analyses on MDC morphogenesis, as we observed a lighter luminal electron density within MDCs distinct from staining observed in adjacent mitochondria and comparable to the surrounding cytosol.

While our results demonstrate that cytosolic GFP is not excluded from MDCs, it remained unclear if MDCs contained openings to the cytosol or if MDCs could fully entrap cytosolic material. To distinguish between these possibilities, we fused the auxin-induced degron to cytosolic GFP (GFP-IAA7), induced MDC formation, and subsequently treated cells with vehicle control or auxin. In vehicle-treated cells, we similarly observed that cytosolic GFP-IAA7 was not excluded from the interior of MDCs (Fig. 6 C). Strikingly, upon auxin treatment, we often observed that the only GFP-IAA7 signal that remained came from the interior of MDCs, demonstrating that MDCs could encase cytosolic GFP-IAA7 and protect it from auxin-induced degradation (Fig. 6 D, white arrow). We observed that cytosolic GFP-IAA7 was protected in both the large spherical MDCs (40% of MDCs) and in the bright, membrane extensions (10% of MDCs, Fig. 6 D) demonstrating that these bright extensions are elongated compartments with captured cytosolic GFP-IAA7. Importantly, we also found that in ∼50% of cases, MDCs could not protect cytosolic GFP-IAA7 from degradation (Fig. 6 D, bottom panels), suggesting that either these MDCs formed after GFP-IAA7 was degraded, GFP-IAA7 can still be degraded inside some MDCs, or that in some instances, openings exist to allow exchange with the cytosol. Additionally, we observed that MDCs formed in response to other stress conditions were also capable of protecting GFP-IAA7 after auxin-induced degradation (Fig. S4 C), except after ConcA treatment, where the auxin-induced degradation system was inhibited for unknown reasons (Fig. S4 C, top panels). Collectively, these results demonstrate that MDCs are a distinct reorganization of OMM, capable of entrapping layers of OMM and cytosolic content.

The mitochondrial fission and fusion machinery perform competing roles in MDC formation

Our results suggest that MDCs form through the repeated elongation and closure of OMM-derived membrane extensions, suggesting that membrane remodeling machinery is involved in MDC biogenesis. To test whether the mitochondrial fission and fusion machinery are involved in MDC formation, we began by determining the localization of the mitochondrial fission and fusion GTPases, Dnm1 and Fzo1, respectively, compared with MDCs (Fig. 7, A–C). Consistent with previous observations, we observed that sfGFP-Dnm1 remains punctate on mitochondrial tubules but also strongly associates with the majority of MDCs upon MDC induction (Fig. 7, A and C; Hughes et al., 2016). Conversely, a functional sfGFP-Fzo1 protein becomes robustly incorporated in 95% of observed MDCs and is present throughout the MDC structure (Fig. 7, B and C). Importantly, while the sfGFP-Fzo1 construct analyzed is overexpressed compared with wild-type Fzo1 (Fig. S5 A), the majority of the sfGFP-Fzo1 is strongly sequestered into MDCs and depleted from the mitochondrial tubule (Fig. 7 B). Because removal of Fzo1 (*fzo1*Δ) generates hyperfragmented mitochondria (Hermann et al., 1998), we assessed the requirement of Fzo1 in MDC formation by analyzing MDC biogenesis in strains lacking *DNM1*, *dnm1*Δ, and *dnm1*Δ*fzo1*Δ yeast, which maintain a tubular mitochondrial morphology. Surprisingly, *dnm1*Δ*fzo1*Δ yeast still robustly formed MDCs in response to both ConcA and Rap treatment (Fig. 7 D) and to a similar extent as was observed in wild-type and *dnm1*Δ cells. The continued formation of MDCs in *dnm1*Δ yeast matched our previous observations that the mitochondrial fission machinery is not required for MDC formation (Hughes et al., 2016). Furthermore, in assessing the structural diversity of MDCs in *dnm1*Δ cells, we observed more MDCs resolving into large spherical domains and compartments compared with wild-type yeast (Fig. 7 E), indicating that Dnm1 may antagonize MDC formation by constricting or severing OMM proliferations before they round into spherical compartments. In *dnm1*Δ*fzo1*Δ cells, the structural diversity of MDCs resembled what we observed in wild-type cells, except that there was a greater proportion of MDCs that formed bright membrane extensions (Fig. 7 E). While these results demonstrate that Fzo1 is not strictly required for MDC formation, they also implied that the role Fzo1 performs in MDC formation might be masked by the complete absence of Dnm1 activity. Thus, we also assessed MDC formation in wild-type, *fzo1*Δ, and *dnm1*Δ*fzo1*Δ yeast that all ectopically expressed either a wild-type Fzo1 protein or a temperature-sensitive version of Fzo1 (*fzo1-1*), both of which are expressed from the *FZO1* promoter and maintained at similar protein levels in cells (Fig. S5 B; Hermann et al., 1998). While MDC formation still occurred in wild-type yeast expressing *fzo1-1* at 37°C, we observed that MDC formation was consistently reduced at higher temperatures because fewer MDCs also formed at 37°C in control cells expressing wild-type Fzo1 (p*FZO1*; Fig. 7, F–H). Conversely, MDC formation was strongly impaired in *fzo1*Δ

Downloaded from http://rupress.org/jcb/article-pdf/223/11/e202307035/1931486/jcb_202307035.pdf by University Colorado Boulder user on 23 October 2024

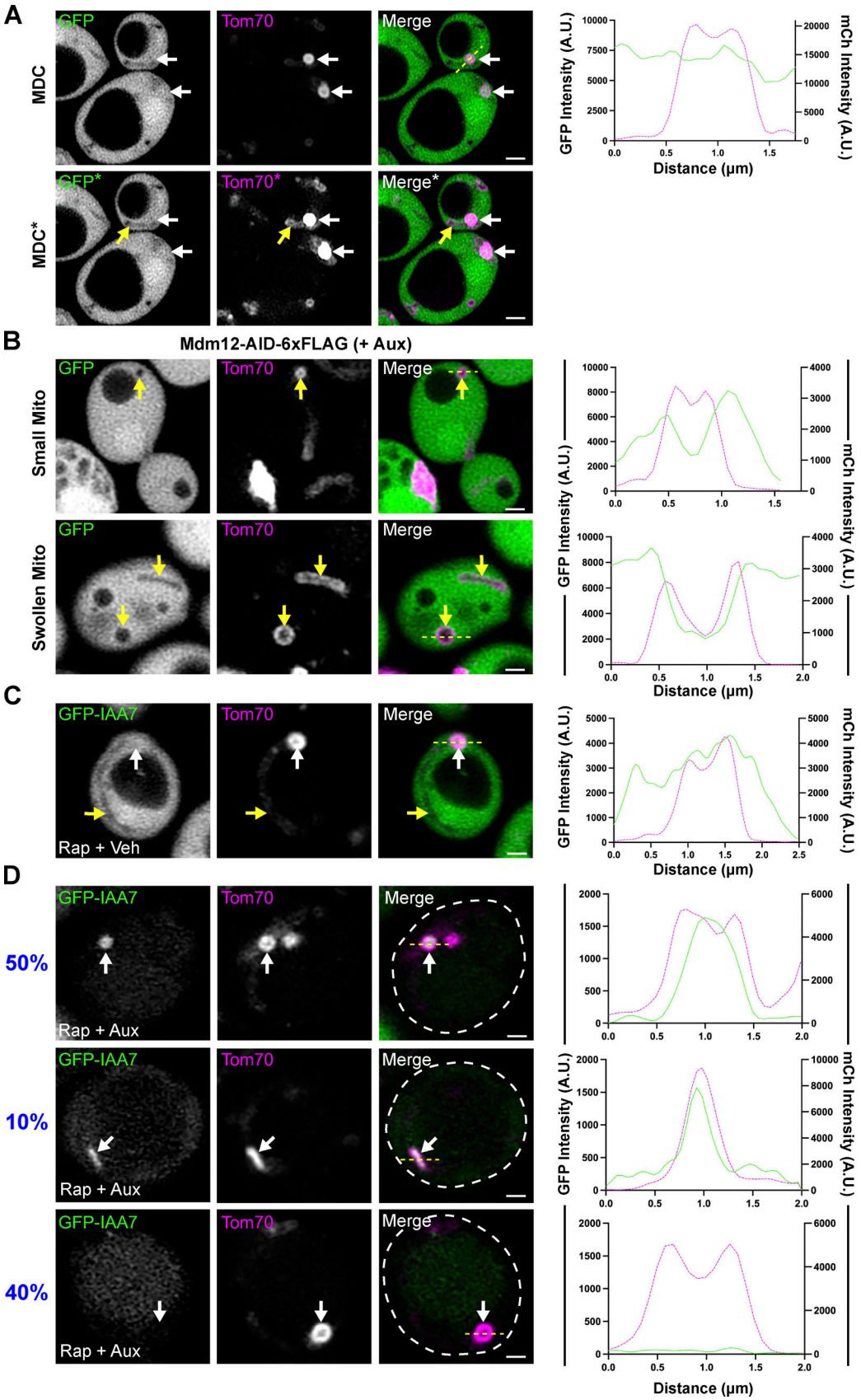

Figure 6. **The MDC lumen contains cytosolic material. (A)** Super-resolution confocal fluorescence microscopy images of Rap-induced MDC formation in yeast expressing yEGFP and Tom70-mCherry. MDCs are indicated by white arrows. Scale bar = 1 μm. The yellow line marks the position of the line-scan fluorescence intensity profile shown to the right. The left and right y axes correspond to yEGFP and Tom70-mCherry fluorescence intensity, respectively.

Downloaded from http://rupress.org/jcb/article-pdf/223/11/e202307035/1931486/jcb_202307035.pdf by University Colorado Boulder user on 23 October 2024

*Panels showing an increased pixel intensity to observe Tom70-mCherry–marked mitochondrial tubules, indicated with a yellow arrow. **(B)** Super-resolution confocal fluorescence microscopy images of swollen mitochondria (yellow arrows) from yeast expressing yEGFP, Tom70-mCherry, Mdm12-AID-6xFLAG, and *Os*Tir1. Images were taken 3 h after treatment with 1 mM auxin, which acutely swelled mitochondria through auxin-induced degradation of Mdm12-AID-6xFLAG. Scale bar = 1 µm. The yellow line marks the position of the line-scan fluorescence intensity profile shown to the right. Left and right y axes correspond to yEGFP and Tom70-mCherry fluorescence intensity, respectively. **(C and D)** Representative super-resolution confocal fluorescence microscopy images of yeast expressing yEGFP-IAA7 and Tom70-mCherry. After a two-hour treatment with 200 nM Rap, cells were subsequently treated with 70% ethanol (C; Rap + Veh) or 1 mM auxin (D; Rap + Auxin). Yellow arrows mark mitochondria while white arrows mark MDCs. Scale bar = 1 µm. The yellow line denotes the position of the line-scan fluorescence intensity profile shown to the right. The left and right y axes correspond to GFP and Tom70-mCherry fluorescence intensity, respectively. The blue percentages next to the panels shown in D indicate the frequency those results were observed from *n* = 106 MDCs from four experiments.

p*fzo1-1* cells after an acute 1-h shift to the non-permissive temperature of 37°C but not at the permissive temperature of 30°C (Fig. 7, F–H). Rather than forming MDCs, we frequently observed puncta containing only Tom70-GFP throughout the cell in *fzo1*Δ p*fzo1-1* cells treated with Rap at 37°C (Fig. 7 G, yellow arrows). These Tom70-GFP puncta did not appear enriched for Tom70-GFP as they were the same fluorescence intensity as that observed for the Tom70-GFP that remained in the fragmented mitochondria and may represent small Tom70-GFP–positive vesicles. Similar to our observations of MDC formation in *dnm1*Δ*fzo1*Δ cells, MDCs formed to a similar extent in *dnm1*Δ*fzo1*Δ p*fzo1-1* cells at both the permissive (30°C) and non-permissive (37°C) temperatures (Fig. 7 H).

To further explore the role the mitochondrial fusion machinery performs in MDC biogenesis, we examined MDC formation in yeast strains where IMM fusion was impaired by inactivating the IMM fusion GTPase Mgm1 (Wong et al., 2000). To do so, we ectopically expressed either a wild-type (p*MGM1*) or temperature-sensitive allele of Mgm1 (p*mgm1-5*) in wild-type, *mgm1*Δ, and *dnm1*Δ*mgm1*Δ yeast and assessed MDC formation after Rap treatment. Notably, each of these yeast strains readily formed MDCs at both the permissive (30°C) and non-permissive (37°C) temperatures in response to Rap treatment (Fig. S5, C–E). Thus, contrary to what we observed upon inhibition of Fzo1, *mgm1*Δ p*mgm1-5* cells formed MDCs to a similar extent at both the permissive (30°C) and non-permissive (37°C) temperatures even though mitochondria aggregate and become more fragmented at the non-permissive (37°C) temperature (Fig. S5 D). Together, these results suggest that the mitochondrial fusion machinery is not absolutely required for MDC formation, but Fzo1 appears to perform a distinct role counteracting the activity of the mitochondrial fission machinery to allow MDCs to form from OMM proliferations.

Discussion

Mitochondria structurally reorganize to meet metabolic demands and, in times of stress, to preserve organelle homeostasis. Defects in mitochondrial dynamics and the observance of aberrant mitochondrial structures are hallmarks of disease states and a phenotype of aging cells (Youle and van der Bliek, 2012; Hughes and Gottschling, 2012). Previously, we identified a new structural domain of mitochondria, the MDC, that forms in aged yeast cells and mammalian cell culture in response to several acute stressors (Hughes et al., 2016; Schuler et al. 2020, *Preprint*; Schuler et al., 2021). Here, we used TEM and electron tomography to determine the ultrastructure of MDCs. We observed that MDCs form as large, multilamellar spherical compartments that frequently encase four membrane bilayers, whereby two closely apposed membrane bilayers form an internal compartment that is surrounded by a second layer of closely apposed double membrane bilayers. We demonstrate that MDCs form through OMM extensions that repeatedly elongate, coalesce, and engulf part of themselves to create these compartments with layers of entrapped membrane. In doing so, MDCs engulf both OMM and cytosolic content, securing cargo into a distinct, protected domain. Overall, these results provide evidence of key features that distinguish MDCs from other previously identified mitochondrial structures and cargo-sorting domains.

Mitochondria form an elaborate architecture constructed by the organization of two membranes. While the OMM establishes the limiting membrane of mitochondria, the IMM surrounds the mitochondrial matrix and invaginates to create cristae, establishing several distinct aqueous and membrane subdomains (Iovine et al., 2021). Several membrane components and protein complexes embedded in the IMM are required to establish IMM architecture (Klecker and Westermann, 2021). Notably, the sharp-angled dimerization and oligomerization of F_1F_O-ATP synthase complexes within the IMM facilitates the generation and maintenance of mitochondrial cristae (Paumard et al., 2002; Davies et al., 2012). In the absence of ATP synthase dimerization, the IMM forms membrane sheets traversing the mitochondrial matrix, creating "onion-like" mitochondria as observed by EM (Paumard et al., 2002; Giraud et al., 2002; Davies et al., 2012). These mitochondria can form swollen spheres that are still delimited by the OMM (Paumard et al., 2002) but can appear to encase cytosol if they form depressed cup-like structures (Klecker and Westermann, 2021). As observed by EM, mitochondria can also form onion-like structures at sites of curved IMM septa (Harner et al., 2016) and in the absence of key organizational complexes, including the mitochondrial contact site and cristae organizing system and ERMES complexes (Stephan et al., 2020; Hobbs et al., 2001). Importantly, the onion-like structures observed in all of these scenarios with alterations of IMM architecture are still surrounded by a single OMM, contain layers of IMM, and still encase mitochondrial matrix. In contrast, the multilamellar compartments we observed forming upon MDC induction contain layers of OMM and are clearly capable of engulfing cytosolic content. Moreover, our previous analyses and observations within an accompanying manuscript all demonstrate that MDCs exclude content from the mitochondrial matrix,

Downloaded from http://rupress.org/jcb/article-pdf/223/11/e202307035/1931486/jcb_202307035.pdf by University Colorado Boulder user on 23 October 2024

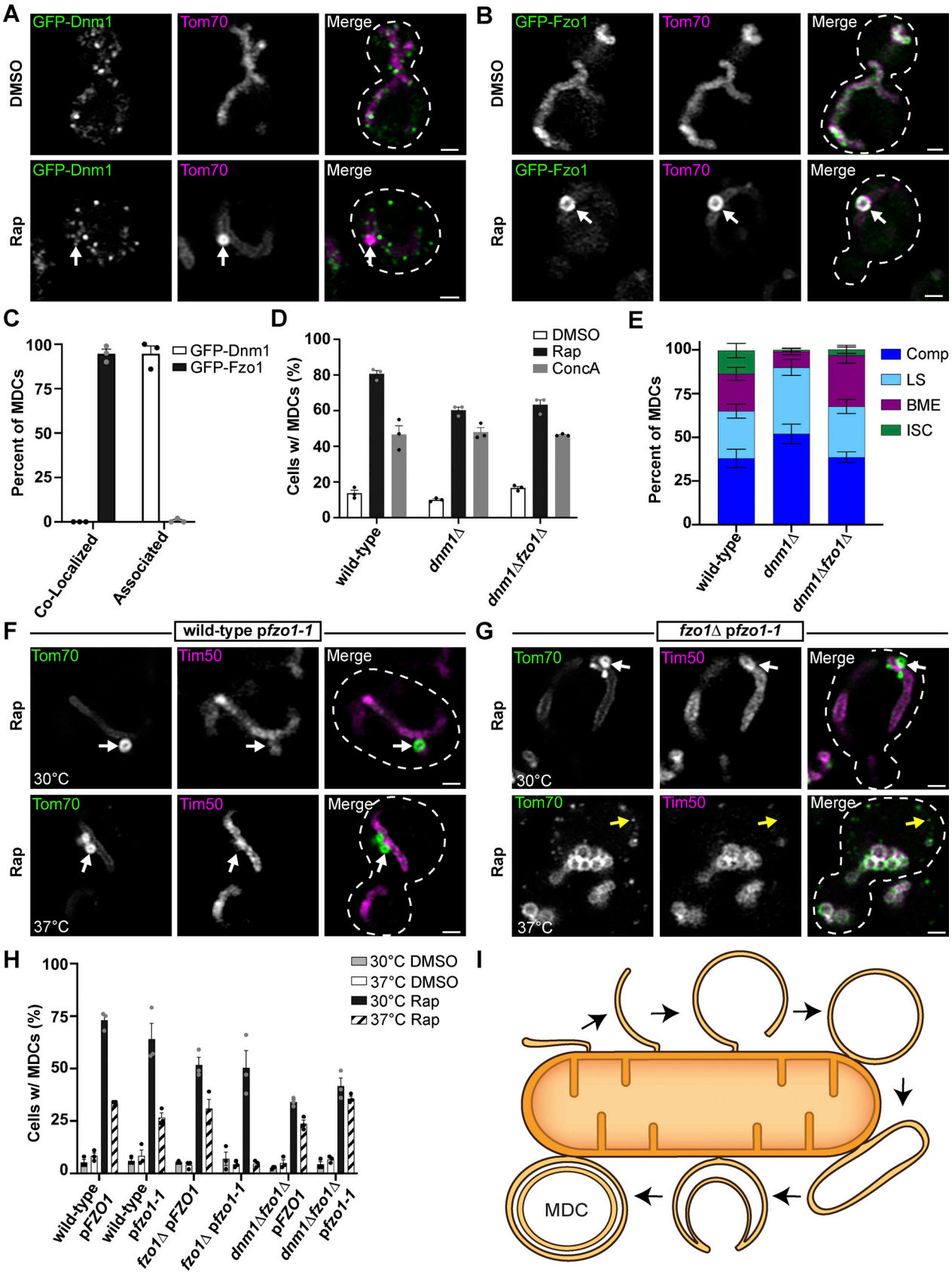

Figure 7. **The mitochondrial fission and fusion machinery perform competing roles in MDC formation. (A)** Super-resolution confocal fluorescence microscopy images of a haploid yeast strain expressing sfGFP-Dnm1 from the *NOP1* promoter and Tom70-mCherry treated with either DMSO or 200 nM Rap. MDCs are indicated by white arrows. Scale bar = 1 µm. **(B)** Super-resolution confocal fluorescence microscopy images of a haploid yeast strain expressing

Downloaded from http://rupress.org/jcb/article-pdf/223/11/e202307035/1931486/jcb_202307035.pdf by University Colorado Boulder user on 23 October 2024

sfGFP-Fzo1 from the *NOP1* promoter and Tom70-mCherry treated with either DMSO or 200 nM Rap. MDCs are indicated by white arrows. Scale bar = 1 µm. **(C)** Quantification of the frequency sfGFP-Dnm1 foci or sfGFP-Fzo1 were co-localized with or closely associated with Tom70-mCherry–marked MDCs. Error bars show mean ± SE of three replicates, $n \geq 100$ cells per replicate. **(D)** Quantification of MDC formation in the indicated yeast strains upon treatment with either DMSO, ConcA, or Rap. Error bars show mean ± SE of three replicates, $n \geq 100$ cells per replicate. **(E)** Quantification of the MDC morphologies observed in the indicated yeast strains after Rap treatment shown as a percent of total MDCs. Error bars show mean ± SE of three replicates, $n \geq 100$ cells per replicate. **(F and G)** Super-resolution confocal fluorescence microscopy images of wild-type (F) or *fzo1Δ* (G) yeast cells expressing *fzo1-1*, Tom70-yEGFP, and Tim50-mCherry treated with 200 nM Rap at the indicated temperatures. MDCs are indicated by white arrows. Yellow arrows in G are pointing to Tom70-yEGFP puncta detached from the mitochondrial tubule. Scale bar = 1 µm. **(H)** Quantification of MDC formation in the indicated yeast strains upon treatment with either DMSO or Rap at the indicated temperatures. Error bars show mean ± SE of three replicates, $n \geq 100$ cells per replicate. **(I)** Model of MDC biogenesis from an OMM extension that forms a double-membrane compartment, elongating and invaginating to form a multilamellar MDC.

the IMM, and the intermembrane space (Hughes et al., 2016; Wilson et al., 2024), which is consistent with our observations of MDC ultrastructure and formation. Thus, while MDCs appear similar to mitochondria with aberrant IMM organization, they are actually a distinct remodeling of the OMM.

Our observations provide a model for how MDCs form through a membrane proliferation that is derived entirely from the OMM (Fig. 7 I). In this model, the generation of MDCs begins with an OMM extension that rounds up and connects to create an initial double-membrane compartment that has engulfed cytosol. This compartment can continue to grow, elongate, and inwardly engulf part of itself and cytosol to create a compartment with layers of OMM encased in a concentric spherical compartment, where each compartment is bound by two closely apposed membrane bilayers. In considering this model for MDC biogenesis, it was surprising to discover that Fzo1 is not strictly required for MDC formation because we predicted that Fzo1 activity may be necessary to either bring the membranes together or drive fusion. This result may indicate that the OMM proliferations do not fuse but instead form tight connections that we could not clearly resolve in our EM analyses. Alternatively, the topology of an OMM extension that encloses and subsequently forms an invaginated internal compartment may require a membrane scission event rather than membrane fusion (Zhen et al., 2021). The loss of MDC formation within *fzo1Δ* p*fzo1-1* cells at non-permissive temperatures suggests that Fzo1 still supports MDC formation by a mechanism that is currently unknown. Based on our genetic experiments, it seems possible that Fzo1 may inhibit Dnm1 from acting on mitochondrial membrane extensions to allow the membrane to round up into an MDC.

While we continue to identify components required for MDC formation (Xiao et al., 2024), it still remains unclear what cellular machinery is mechanistically involved in forming MDCs. The large size and shape of MDCs strongly suggest that cytoskeletal machinery is required to provide both a force to drive OMM extensions and to support the bending and shaping of the OMM into MDCs. In support, our model for MDC formation is similar to the bending and closure of the isolation membrane during autophagosome formation, a process that involves the actin cytoskeleton (Kast et al., 2015; Mi et al., 2015). Furthermore, it is noticeable in our electron tomography that we frequently observed close contact between MDCs and the ER, and we have previously identified that ERMES and the conserved Miro GTPase Gem1 are both necessary for MDC formation (English et al., 2020). Considering both ERMES and the mammalian orthologs of Gem1 (Miro1 and Miro2) are implicated in connecting mitochondria to the actin cytoskeleton (or microtubules in the case of Miro1 and Miro1) (Boldogh et al., 1998; López-Doménech et al., 2018), it seems possible that Gem1 and the ER facilitate MDC formation by recruiting cytoskeletal machinery to the OMM to support the extension and shaping of OMM into MDCs.

There are notable similarities between the MDC pathway and ER microautophagy. ER microautophagy can be induced by the overexpression of some resident ER membrane proteins, by ER stress, or by the aberrant retention of membrane proteins within the organelle (Wright et al., 1988; Schuck et al., 2009; Schäfer et al., 2020). The accumulation of these membrane proteins induces a dramatic proliferation of ER membranes that stack together as paired membrane doublets around the nucleus or in the cell periphery, which can round into multilamellar whorls (Wright et al., 1988; Koning et al., 1996; Schuck et al., 2014). Subsequently, this distinct ER domain is degraded in vacuoles/lysosomes in a manner that does not rely on the core autophagy machinery (Schuck et al., 2014). Prompted by these similarities, we observed in an accompanying manuscript that MDCs are also induced by the overexpression of many OMM proteins and by the mistargeting of tail-anchored membrane proteins to the OMM (Wilson et al., 2024). Here, we show that MDCs, similar to ER microautophagy, form from a mitochondrial OMM proliferation to create a distinct membrane domain formed by closely apposed, paired membrane bilayers, indicating that mitochondria can also generate dramatic membrane proliferations as a means to sequester content from the organelle.

Extensions, protrusions, and vesicles derived from the OMM have been observed in multiple cell types under both steady-state and pathological conditions (Soubannier et al., 2012a; Yao et al., 2020; Yamashita et al., 2016). Under mild stress conditions, mitochondria can release small vesicles (MDVs) that contain only the OMM or both mitochondrial membranes, delivering damaged protein cargoes, including intramitochondrial protein cargoes, to lysosomes for degradation (Soubannier et al., 2012a). Thus far, we have considered MDCs to be distinct from MDVs based on their size, mechanism of formation, and cargo proteins sequestered. The observations presented here further support that distinction, highlighted by our results showing that MDCs are OMM-enriched multilamellar compartments that engulf both OMM and cytosol. It seems possible that MDCs may provide cells a mechanism to sequester portions of the OMM or other cellular content that cannot be achieved by creating MDVs that are still delimited by the OMM. Interestingly, a recent study

Downloaded from http://rupress.org/jcb/article-pdf/223/11/e202307035/1931486/jcb_202307035.pdf by University Colorado Boulder user on 23 October 2024

demonstrated that upon *Toxoplasma gondii* infection, the targeting of the pathogen protein *Tg*MAF1 to the OMM induced mitochondria to shed their outer membrane, creating large ring-shaped structures, called structures positive for the outer membrane (SPOTs). These SPOTs robustly incorporated some OMM membrane proteins, while excluding intramitochondrial proteins, and included internal invaginations that were also morphologically reminiscent of ER whorls (Li et al., 2022). While it is currently unclear how SPOTs form, it would be interesting if they also form by invaginating OMM extensions and engulfing cytoplasmic material, similar to what we observed for MDC biogenesis. Altogether, it is clear that the remodeling of the OMM is a key mechanism by which cells preserve mitochondrial homeostasis. Understanding heterogenous molecular mechanisms of this remodeling may provide new avenues to target pathological states that disrupt mitochondrial architecture.

Materials and methods

Yeast strains and plasmids

All yeast strains are derivatives of *Saccharomyces cerevisiae* S288C (BY) (Brachmann et al., 1998) and are listed in Table S1. Deletion strains were created by one-step PCR-mediated gene replacement using the previously described pRS series of vectors (Brachmann et al., 1998; Sikorski and Hieter, 1989) and oligo pairs listed in Table S2. Correct gene deletions were confirmed by colony PCR across the chromosomal insertion site. Strains expressing proteins with attached C-terminal fluorescent proteins were created by one-step PCR-mediated C-terminal endogenous epitope tagging using standard techniques and oligo pairs listed in Table S2. Plasmid templates for fluorescent epitope tagging were from the pKT series of vectors (Sheff and Thorn, 2004). Strains containing auxin-inducible degrons were constructed as described in the Auxin-induced protein degradation section below. For all strains, correct integrations were confirmed by a combination of colony PCR across the chromosomal insertion site and correctly localized expression of the fluorophore by microscopy. Strains expressing proteins with attached N-terminal fluorescent proteins were derived from the SWAp-Tag library described in Weill et al. (2018) and were a gift from Maya Schuldiner. The plasmids used in this study are listed in Table S3. To generate a plasmid expressing the temperature-sensitive *mgm1-5* allele, the *mgm1-5* ORF plus ~500 base pairs upstream (5′UTR) and downstream (3′UTR) were PCR amplified from JFY4629 genomic DNA and contained flanking regions with either a Xho1 or Not1 recognition site. This *mgm1-5* amplicon was inserted into the pRS315 plasmid linearized by digestion with Xho1 and Not1 and the plasmids were reassembled through ligation with the *mgm1-5* locus also digested with Xho1 and Not1. Sequencing confirmed the G409D mutation of the *mgm1-5* allele.

Yeast cell culture and growth assays

Yeast cells were grown exponentially for 15–16 h at 30°C to a final optical (wavelength 600 nm) density of 0.5–1 before the start of all experiments. This period of overnight log-phase growth was carried out to ensure vacuolar and mitochondrial uniformity across the cell population and is essential for consistent MDC formation. Unless otherwise indicated, cells were cultured in YPAD medium (1% yeast extract, 2% peptone, 0.005% adenine, 2% glucose). Otherwise, cells were cultured in a synthetic defined (SD) medium that contained the following unless specific nutrients were removed to select for growth or plasmid retention: 0.67% yeast nitrogen base without amino acids, 2% glucose, supplemented nutrients 0.072 g/L each adenine, alanine, arginine, asparagine, aspartic acid, cysteine, glutamic acid, glutamine, glycine, histidine, myo-inositol, isoleucine, lysine, methionine, phenylalanine, proline, serine, threonine, tryptophan, tyrosine, uracil, valine, 0.369 g/L leucine, and 0.007 g/L para-aminobenzoic acid. Unless otherwise indicated, Rap, ConcA, CHX, and auxin were added to cultures at final concentrations of 200 nM, 500 nM, 10 µg/mL, and 1 mM, respectively.

MDC assays

For MDC assays, overnight log-phase cell cultures were grown in the presence of dimethyl sulfoxide (DMSO) or the indicated drug for 2 h. For MDC assays with cells containing plasmids, overnight log-phase yeast cultures grown in selective SD medium were back-diluted to an OD_{600} = 0.1–0.2 in YPAD medium and allowed to grow for at least 4 h prior to MDC induction. For the temperature-sensitive MDC assays, cultures were shifted to the indicated temperatures 1 h prior to MDC induction. Prior to visualization, cells were harvested by centrifugation, washed once, and resuspended in 100 mM HEPES containing 5% glucose. Subsequently, yeast were directly plated onto a slide at small volumes to allow the formation of a monolayer, and optical z-sections of live yeast cells were acquired with a ZEISS Axio Imager M2 or for super-resolution confocal fluorescence microscopy images a ZEISS LSM800 with Airyscan was used. The percentage of cells with MDCs were quantified in each experiment at the 2 h time point. All quantifications show the mean ± SE from three biological replicates with n = 100 cells per experiment. MDCs were identified as Tom70-positive, Tim50-negative structures that were enriched for Tom70 versus the mitochondrial tubule. In MDC colocalization assays, MDCs were identified as large, Tom70-enriched, spherical structures prior to assessing the colocalization of different proteins of interest.

Fluorescence microscopy

Fluorescence microscopy was performed as described in English et al. (2020). In brief, optical z-sections of live yeast cells were acquired with a ZEISS Axio Imager M2 equipped with a ZEISS Axiocam 506 monochromatic camera, 100× oil-immersion objective (plan apochromat, NA 1.4) or 63× oil-immersion objective (plan apochromat, NA 1.4) or a ZEISS LSM800 equipped with an Airyscan detector, 63× oil-immersion objective (plan apochromat, NA 1.4) at room temperature. Time-lapse fluorescence microscopy imaging was also performed as described in English et al. (2020). Briefly, overnight log-phase cultures were treated with 1 µM Rap for 15 min, harvested by centrifugation, resuspended in SD medium, and pipetted into flow chamber slides as previously described (English et al., 2020). Optical z-sections of live yeast cells were acquired with a ZEISS Airyscan LSM880

Downloaded from http://rupress.org/jcb/article-pdf/223/11/e202307035/1931486/jcb_202307035.pdf by University Colorado Boulder user on 23 October 2024

equipped with an environmental chamber set to 30°C. Widefield images were acquired with ZEN (Carl Zeiss) and processed with Fiji (Schindelin et al., 2012). Time-lapse images and super-resolution images were acquired with ZEN (Carl Zeiss) and processed using the automated Airyscan processing algorithm in ZEN (Carl Zeiss) and further processed in Fiji. Fluorochromes are indicated in figure legends. Individual channels of all images were minimally adjusted in Fiji to match the fluorescence intensities between channels for better visualization. Line-scan analysis was performed on non-adjusted, single z-sections in Fiji.

TEM and electron tomography

Yeast cells were high-pressure frozen and freeze-substituted as previously described (Wilson et al., 2021). Liquid cultures of yeast cells were harvested at the mid-logarithmic phase, vacuum filtered on 0.45-µm millipore paper, loaded into 0.5-mm aluminum hats, and high-pressure frozen with a Wohlwend HPF (Wohlwend). Cells were freeze-substituted in an Automated Freeze-Substitution machine at −90°C in an en bloc preparation of 0.1% uranyl acetate and 0.25% glutaraldehyde in anhydrous acetone. Samples were then washed in pure anhydrous acetone, embedded in Lowicryl HM20 resin (Polysciences), UV polymerized at −60°C warming slowly over 4 days to room temperature (RT). The sample blocks were then stored at −20°C. These methods preserve membrane and protein structure and provide consistent en bloc staining for immuno-EM membrane identification (Giddings, 2003).

A Leica UC6 Ultra-Microtome was used to cut and place serial sections on Formvar-coated rhodium-plated copper slot grids (Electron Microscopy Sciences). 80–90-nm serial sections were cut for TEM, and immuno-EM experiments and 200-nm-thick serial sections were cut for dual-axis tomography. For immunolabeling experiments, grids were exposed to sequential 50-µl droplets: nonspecific antibody binding was blocked by incubation with 1% PBS + 1% dry milk (blocking solution) for 20 min at RT, then exposed to primary antibodies overnight at 4°C (1:500 anti-GFP) in blocking solution, washed at RT in 1% PBS with three sequential 50-µl drops, labeled with a secondary anti-rabbit or anti-mouse gold (depending on the primary antibody used) at RT for 1 h (1:200 goat-anti-rabbit or goat-anti-mouse; Electron Microscopy Sciences), washed in 1% PBS with three sequential 50-µl drops, and finally washed in distilled water with two sequential 50-µl drops.

Thin cell sections were imaged with a FEI Tecnai T12 Spirit electron microscope equipped with a 120 kV LaB6 filament and AMT (2 × 2 k) CCD. TEM of hundreds of cells per strain was used to quality control freezing, embedding, and staining. Thick sections were labeled with fiduciary 15-nm colloidal gold (British Biocell International) on both sides and tilt-imaged with a Tecnai 30 (f-30, 300 kV; FEI-Company) with dual-tilt series images collected from +60° to −60° with 1.5° increments using a Gatan US4000 4 × 4 k CCD camera (Abingdon). The tilt series were imaged primarily at 19,000× magnification and repeated with a 90° rotation for dual-axis tomography (Mastronarde 1997). Tomograms were built and modeled using the IMOD software package (Kremer et al., 1996) using an iMac (Apple). MDC, mitochondria, and ER membrane models from dual-axis electron tomograms, and immuno-tomograms were manually assigned from the outer leaflet every 5 nm. Immunogold was modeled at the same size as secondary gold (6-nm anti-mouse and 10-nm anti-rabbit; Electron Microscopy Sciences) and colored similarly to the closest membrane as indicated in the figure legends. Videos were made using IMOD and QuickTime Pro (Apple). Data were analyzed and graphed using Prism 9 (GraphPad).

Protein preparation and immunoblotting

For western blot analysis of protein levels, yeast cultures were grown to log-phase (OD_{600} = 0.5–1) and two OD_{600} cell equivalents were isolated by centrifugation, washed with distilled water, and incubated in 0.1 M NaOH for 5 min at RT. Subsequently, cells were reisolated by centrifugation at 16,000 × *g* for 10 min at 4°C and lysed for 5 min at 95°C in lysis buffer (10 mM Tris pH 6.8, 100 mM NaCl, 1 mM EDTA, 1 mM EGTA, 1% SDS and containing cOMPLETE protease inhibitor cocktail [Millipore Sigma]). Upon lysis, samples were denatured in Laemmli buffer (63 mM Tris pH 6.8, 2% SDS, 10% glycerol, 1 mg/ml bromophenol blue, 1% β-mercaptoethanol) for 5 min at 95°C. To separate proteins based on molecular weight, equal amounts of protein were subjected to SDS polyacrylamide gel electrophoresis and transferred to nitrocellulose membrane (Millipore Sigma) by semi-dry transfer. Nonspecific antibody binding was blocked by incubation with Tris-buffered saline + 0.05% Tween-20 (TBST) containing 10% dry milk (Sigma-Aldrich) for 1 h at RT. After incubation with the primary antibodies at 4°C overnight, membranes were washed four times with TBST and incubated with secondary antibody (goat-anti-rabbit or donkey-anti-mouse HRP-conjugated,1:5,000 in TBST + 10% dry milk; Sigma-Aldrich) for 1 h at RT. Subsequently, the membranes were washed twice with TBST and twice with TBS, enhanced chemiluminescence solution (Thermo Fisher Scientific) was applied and the antibody signal was detected with a BioRad Chemidoc MP system. All blots were exported as TIFFs and cropped in Adobe Photoshop CC.

Auxin-induced protein degradation

Auxin-induced protein degradation was performed essentially as described in Shetty et al. (2019) except 3-indole acetic acid (auxin) was added to a final concentration of 1 mM at the 0-time point in all experiments. All yeast strains containing the auxin-inducible degron, IAA7, were generated by endogenous C-terminal integration of yEGFP-IAA7 PCR amplified from a plasmid created for this study (Table S3) by removing 3V5 from the plasmid described in Eng et al. (2014) by cutting with Pac1/Xba1 and replacing with yEGFP cut with similar restriction enzymes, except Mdm12, which was C-terminally fused to AID*-6xFLAG from the constructs described in Morawska and Ulrich (2013). Subsequently, GPD1-OsTIR1 was integrated into the *LEU2* locus using the plasmid pNH605-pGPD1-osTIR1 digested with Swa1 as described in Chan et al. (2018). Auxin-induced protein degradation was followed by both immunoblotting from whole cell extracts and fluorescence microscopy as described above.

Quantification and statistical analysis

The number of replicates, what *n* represents, and dispersion and precision measures are indicated in the figure legends. In

Downloaded from http://rupress.org/jcb/article-pdf/223/11/e202307035/1931486/jcb_202307035.pdf by University Colorado Boulder user on 23 October 2024

general, quantifications show the mean ± SE from three biological replicates with n = 100 cells per experiment. In experiments with data depicted from a single biological replicate, the experiment was repeated with the same results.

Contact for reagent and resource sharing

Further information and requests for resources and reagents should be directed to and will be fulfilled by the lead contact, Adam Hughes. All unique/stable reagents generated in this study are available from the lead contact without restrictions.

Online supplemental material

Fig. S1 shows that ConcA treatment also induces mitochondria to produce mitochondrial-associated multilamellar structures. Fig. S2 provides evidence that MDCs are not bound by autophagosomal membranes. Fig. S3 contains stills of time-lapse imaging of MDC biogenesis during Rap, ConcA, and CHX, all demonstrating that MDCs form from repeated membrane extension and engulfment events. Fig. S4 shows that MDCs induced by a variety of stress conditions contain cytosol within the MDC lumen. Fig. S5 demonstrates that the IMM GTPase Mgm1 is not required for MDC formation. Table S1 lists the yeast strains used in this study. Table S2 lists the oligonucleotides used in this study. Table S3 lists bacterial strains, chemicals, antibodies, plasmids, and software used in this study. Video 1 (related to Fig. 2) shows mitochondrial-derived multilamellar structures are enriched for Tom70-GFP and exclude Tim50-mCherry. Video 2 (related to Fig. 3, A–C) shows mitochondrial-derived compartments contain sets of paired membranes. Video 3 (related to Fig. 3, D–F) shows mitochondrial-derived compartments contain sets of paired membranes. Video 4 (related to Fig. 3, G–I) shows mitochondrial-derived compartments contain sets of paired membranes. Video 5 (related to Fig. 4 A) shows mitochondrial-derived compartments form through membrane extension intermediates. Video 6 (related to Fig. 4 C) shows mitochondrial-derived compartments form through membrane extension intermediates. Video 7 (related to Fig. S2) shows mitochondrial-derived compartments contain sets of paired membranes. Video 8 (related to Fig. S3 A) shows mitochondrial-derived compartments form through membrane extension intermediates. Video 9 (related to Fig. S3 B) shows mitochondrial-derived compartments form through membrane extension intermediates. Video 10 (related to Fig. S3 D) shows mitochondrial-derived compartments form through membrane extension intermediates.

Data availability

All reagents used in this study are available upon request. All other data reported in this paper will be shared by the lead contact upon request. This paper does not report original code. Any additional information required to reanalyze the data reported in this paper is available from the lead contact upon request.

Acknowledgments

We thank members of the A.L. Hughes and G. Odorizzi groups for discussion and manuscript comments. We thank members of the Janet M. Shaw (University of Utah, Salt Lake City, UT, USA) laboratory for providing reagents and plasmids for this project. We also thank Maya Schuldiner (Weizmann Institute of Science, Rehovot, Israel) for gifting the yeast SWAp-Tag library described in Weill et al. (2018) and Jonathan Friedman (University of Texas Southwestern Medical Center, Dallas, TX, USA) for gifting yeast strains.

Z.N. Wilson, PhD, was supported by an American Heart Association Postdoctoral Fellowship, 20POST35200110, and an American Cancer Society–Give Mas, Live Mas Southern Multifoods Postdoctoral Fellowship, PF-20-018-01-CCG. Support for this research was also generously provided by grant number PF-19-0209 from the United Mitochondrial Disease Foundation (Z.N. Wilsson) and National Institutes of Health grants T32GM007464 (A.M. English), R35 GM149202 (G. Odorizzi), GM119694 (A.L. Hughes), and AG061376 (A.L. Hughes).

Author contributions: Z.N. Wilson: Conceptualization, Data curation, Formal analysis, Funding acquisition, Investigation, Methodology, Project administration, Supervision, Validation, Visualization, Writing—original draft, Writing—review & editing, M. West: Formal analysis, Investigation, A.M. English: Investigation, G. Odorizzi: Funding acquisition, Project administration, Supervision, A.L. Hughes: Conceptualization, Funding acquisition, Project administration, Supervision, Writing—review & editing.

Disclosures: The authors declare no competing interests exist.

Submitted: 7 July 2023
Revised: 24 May 2024
Accepted: 17 July 2024

References

Brachmann, C.B., A. Davies, G.J. Cost, E. Caputo, J. Li, P. Hieter, and J.D. Boeke. 1998. Designer deletion strains derived from Saccharomyces cerevisiae S288C: A useful set of strains and plasmids for PCR-mediated gene disruption and other applications. *Yeast*. 14:115–132. https://doi.org/10.1002/(SICI)1097-0061(19980130)14:2<115::AID-YEA204>3.0.CO;2-2

Boldogh, I., N. Vojtov, S. Karmon, and L.A. Pon. 1998. Interaction between mitochondria and the actin cytoskeleton in budding yeast requires two integral mitochondrial outer membrane proteins, Mmm1p and Mdm10p. *J. Cell Biol.* 141:1371–1381. https://doi.org/10.1083/jcb.141.6.1371

Chan, L.Y., C.F. Mugler, S. Heinrich, P. Vallotton, and K. Weis. 2018. Non-invasive measurement of mRNA decay reveals translation initiation as the major determinant of mRNA stability. *Elife*. 7:e32536. https://doi.org/10.7554/eLife.32536

Davies, K.M., C. Anselmi, I. Wittig, J.D. Faraldo-Gómez, and W. Kühlbrandt. 2012. Structure of the yeast F1Fo-ATP synthase dimer and its role in shaping the mitochondrial cristae. *Proc. Natl. Acad. Sci. USA*. 109:13602–13607. https://doi.org/10.1073/pnas.1204593109

Eng, T., V. Guacci, and D. Koshland. 2014. ROCC, a conserved region in cohesin's Mcd1 subunit, is essential for the proper regulation of the maintenance of cohesion and establishment of condensation. *Mol. Biol. Cell*. 25:2351–2364. https://doi.org/10.1091/mbc.e14-04-0929

English, A.M., M.H. Schuler, T. Xiao, B. Kornmann, J.M. Shaw, and A.L. Hughes. 2020. ER-mitochondria contacts promote mitochondrial-derived compartment biogenesis. *J. Cell Biol.* 219:e202002144. https://doi.org/10.1083/jcb.202002144

Esteban-Martínez, L., E. Sierra-Filardi, R.S. McGreal, M. Salazar-Roa, G. Mariño, E. Seco, S. Durand, D. Enot, O. Graña, M. Malumbres, et al. 2017. Programmed mitophagy is essential for the glycolytic switch during cell differentiation. *EMBO J.* 36:1688–1706. https://doi.org/10.15252/embj.201695916

Downloaded from http://rupress.org/jcb/article-pdf/223/11/e202307035/1931486/jcb_202307035.pdf by University Colorado Boulder user on 23 October 2024

Giddings, T.H. 2003. Freeze-substitution protocols for improved visualization of membranes in high-pressure frozen samples. *J. Microsc.* 212: 53–61. https://doi.org/10.1046/j.1365-2818.2003.01228.x

Giraud, M.F., P. Paumard, V. Soubannier, J. Vaillier, G. Arselin, B. Salin, J. Schaeffer, D. Brèthes, J.P. di Rago, and J. Velours. 2002. Is there a relationship between the supramolecular organization of the mitochondrial ATP synthase and the formation of cristae? *Biochim. Biophys. Acta.* 1555:174–180. https://doi.org/10.1016/s0005-2728(02)00274-8

Hackenbrock, C.R. 1966. Ultrastructural bases for metabolically linked mechanical activity in mitochondria. I. Reversible ultrastructural changes with change in metabolic steady state in isolated liver mitochondria. *J. Cell Biol.* 30:269–297. https://doi.org/10.1083/jcb.30.2.269

Hailey, D.W., A.S. Rambold, P. Satpute-Krishnan, K. Mitra, R. Sougrat, P.K. Kim, and J. Lippincott-Schwartz. 2010. Mitochondria supply membranes for autophagosome biogenesis during starvation. *Cell.* 141: 656–667. https://doi.org/10.1016/j.cell.2010.04.009

Hamasaki, M., N. Furuta, A. Matsuda, A. Nezu, A. Yamamoto, N. Fujita, H. Oomori, T. Noda, T. Haraguchi, Y. Hiraoka, et al. 2013. Autophagosomes form at ER-mitochondria contact sites. *Nature.* 495:389–393. https://doi.org/10.1038/nature11910

Harner, M.E., A.K. Unger, W.J. Geerts, M. Mari, T. Izawa, M. Stenger, S. Geimer, F. Reggiori, B. Westermann, and W. Neupert. 2016. An evidence based hypothesis on the existence of two pathways of mitochondrial crista formation. *Elife.* 5:e18853. https://doi.org/10.7554/eLife.18853

Harper, C.S., A.J. White, and L.L. Lackner. 2020. The multifunctional nature of mitochondrial contact site proteins. *Curr. Opin. Cell Biol.* 65:58–65. https://doi.org/10.1016/j.ceb.2020.02.010

Hermann, G.J., J.W. Thatcher, J.P. Mills, K.G. Hales, M.T. Fuller, J. Nunnari, and J.M. Shaw. 1998. Mitochondrial fusion in yeast requires the transmembrane GTPase Fzo1p. *J. Cell Biol.* 143:359–373. https://doi.org/10.1083/jcb.143.2.359

Hobbs, A.E.A., M. Srinivasan, J.M. McCaffery, and R.E. Jensen. 2001. Mmm1p, a mitochondrial outer membrane protein, is connected to mitochondrial DNA (mtDNA) nucleoids and required for mtDNA stability. *J. Cell Biol.* 152:401–410. https://doi.org/10.1083/jcb.152.2.401

Hughes, A.L., and D.E. Gottschling. 2012. An early age increase in vacuolar pH limits mitochondrial function and lifespan in yeast. *Nature.* 492: 261–265. https://doi.org/10.1038/nature11654

Hughes, A.L., C.E. Hughes, K.A. Henderson, N. Yazvenko, and D.E. Gottschling. 2016. Selective sorting and destruction of mitochondrial membrane proteins in aged yeast. *Elife.* 5:e13943. https://doi.org/10.7554/eLife.13943

Iovine, J.C., S.M. Claypool, and N.N. Alder. 2021. Mitochondrial compartmentalization: Emerging themes in structure and function. *Trends Biochem. Sci.* 46:902–917. https://doi.org/10.1016/j.tibs.2021.06.003

John Peter, A.T., C. Petrungaro, M. Peter, and B. Kornmann. 2022. METALIC reveals interorganelle lipid flux in live cells by enzymatic mass tagging. *Nat. Cell Biol.* 24:996–1004. https://doi.org/10.1038/s41556-022-00917-9

Kanki, T., and D.J. Klionsky. 2008. Mitophagy in yeast occurs through a selective mechanism. *J. Biol. Chem.* 283:32386–32393. https://doi.org/10.1074/jbc.M802403200

Kast, D.J., A.L. Zajac, E.L. Holzbaur, E.M. Ostap, and R. Dominguez. 2015. WHAMM directs the Arp2/3 complex to the ER for autophagosome biogenesis through an actin comet tail mechanism. *Curr. Biol.* 25: 1791–1797. https://doi.org/10.1016/j.cub.2015.05.042

Killackey, S.A., D.J. Philpott, and S.E. Girardin. 2020. Mitophagy pathways in health and disease. *J. Cell Biol.* 219:e202004029. https://doi.org/10.1083/jcb.202004029

Klecker, T., and B. Westermann. 2021. Pathways shaping the mitochondrial inner membrane. *Open Biol.* 11:210238. https://doi.org/10.1098/rsob.210238

Kondadi, A.K., R. Anand, S. Hänsch, J. Urbach, T. Zobel, D.M. Wolf, M. Segawa, M. Liesa, O.S. Shirihai, S. Weidtkamp-Peters, and A.S. Reichert. 2020a. Cristae undergo continuous cycles of membrane remodelling in a MICOS-dependent manner. *EMBO Rep.* 21:e49776. https://doi.org/10.15252/embr.201949776

Kondadi, A.K., R. Anand, and A.S. Reichert. 2020b. Cristae membrane dynamics–a paradigm change. *Trends Cell Biol.* 30:923–936. https://doi.org/10.1016/j.tcb.2020.08.008

Kondapalli, C., A. Kazlauskaite, N. Zhang, H.I. Woodroof, D.G. Campbell, R. Gourlay, L. Burchell, H. Walden, T.J. Macartney, M. Deak, et al. 2012. PINK1 is activated by mitochondrial membrane potential depolarization and stimulates Parkin E3 ligase activity by phosphorylating Serine 65. *Open Biol.* 2:120080. https://doi.org/10.1098/rsob.120080

König, T., H. Nolte, M.J. Aaltonen, T. Tatsuta, M. Krols, T. Stroh, T. Langer, and H.M. McBride. 2021. MIROs and DRP1 drive mitochondrial-derived vesicle biogenesis and promote quality control. *Nat. Cell Biol.* 23: 1271–1286. https://doi.org/10.1038/s41556-021-00798-4

Koning, A.J., C.J. Roberts, and R.L. Wright. 1996. Different subcellular localization of Saccharomyces cerevisiae HMG-CoA reductase isozymes at elevated levels corresponds to distinct endoplasmic reticulum membrane proliferations. *Mol. Biol. Cell.* 7:769–789. https://doi.org/10.1091/mbc.7.5.769

Kremer, J.R., D.N. Mastronarde, and J.R. McIntosh. 1996. Computer visualization of three-dimensional image data using IMOD. *J. Struct. Biol.* 116: 71–76. https://doi.org/10.1006/jsbi.1996.0013

Lazarou, M., S.M. Jin, L.A. Kane, and R.J. Youle. 2012. Role of PINK1 binding to the TOM complex and alternate intracellular membranes in recruitment and activation of the E3 ligase Parkin. *Dev. Cell.* 22:320–333. https://doi.org/10.1016/j.devcel.2011.12.014

Li, X., J. Straub, T.C. Medeiros, C. Mehra, F. den Brave, E. Peker, I. Atanassov, K. Stillger, J.B. Michaelis, E. Burbridge, et al. 2022. Mitochondria shed their outer membrane in response to infection-induced stress. *Science.* 375:eabi4343. https://doi.org/10.1126/science.abi4343

López-Doménech, G., C. Covill-Cooke, D. Ivankovic, E.F. Halff, D.F. Sheehan, R. Norkett, N. Birsa, and J.T. Kittler. 2018. Miro proteins coordinate microtubule- and actin-dependent mitochondrial transport and distribution. *EMBO J.* 37:321–336. https://doi.org/10.15252/embj.201696380

Mastronarde, D.N. 1997. Dual-axis tomography: An approach with alignment methods that preserve resolution. *J. Struct. Biol.* 120:343–352. https://doi.org/10.1006/jsbi.1997.3919

McLelland, G.L., V. Soubannier, C.X. Chen, H.M. McBride, and E.A. Fon. 2014. Parkin and PINK1 function in a vesicular trafficking pathway regulating mitochondrial quality control. *EMBO J.* 33:282–295. https://doi.org/10.1002/embj.201385902

Mi, N., Y. Chen, S. Wang, M. Chen, M. Zhao, G. Yang, M. Ma, Q. Su, S. Luo, J. Shi, et al. 2015. CapZ regulates autophagosomal membrane shaping by promoting actin assembly inside the isolation membrane. *Nat. Cell Biol.* 17:1112–1123. https://doi.org/10.1038/ncb3215

Morawska, M., and H.D. Ulrich. 2013. An expanded tool kit for the auxin-inducible degron system in budding yeast. *Yeast.* 30:341–351. https://doi.org/10.1002/yea.2967

Nishimura, K., T. Fukagawa, H. Takisawa, T. Kakimoto, and M. Kanemaki. 2009. An auxin-based degron system for the rapid depletion of proteins in nonplant cells. *Nat. Methods.* 6:917–922. https://doi.org/10.1038/nmeth.1401

Onishi, M., K. Yamano, M. Sato, N. Matsuda, and K. Okamoto. 2021. Molecular mechanisms and physiological functions of mitophagy. *EMBO J.* 40: e104705. https://doi.org/10.15252/embj.2020104705

Palikaras, K., E. Lionaki, and N. Tavernarakis. 2018. Mechanisms of mitophagy in cellular homeostasis, physiology and pathology. *Nat. Cell Biol.* 20:1013–1022. https://doi.org/10.1038/s41556-018-0176-2

Paumard, P., J. Vaillier, B. Coulary, J. Schaeffer, V. Soubannier, D.M. Mueller, D. Brèthes, J.P. di Rago, and J. Velours. 2002. The ATP synthase is involved in generating mitochondrial cristae morphology. *EMBO J.* 21: 221–230. https://doi.org/10.1093/emboj/21.3.221

Pfanner, N., B. Warscheid, and N. Wiedemann. 2019. Mitochondrial proteins: From biogenesis to functional networks. *Nat. Rev. Mol. Cell Biol.* 20: 267–284. https://doi.org/10.1038/s41580-018-0092-0

Pickles, S., P. Vigié, and R.J. Youle. 2018. Mitophagy and quality control mechanisms in mitochondrial maintenance. *Curr. Biol.* 28:R170–R185. https://doi.org/10.1016/j.cub.2018.01.004

Schäfer, J.A., J.P. Schessner, P.W. Bircham, T. Tsuji, C. Funaya, O. Pajonk, K. Schaeff, G. Ruffini, D. Papagiannidis, M. Knop, et al. 2020. ESCRT machinery mediates selective microautophagy of endoplasmic reticulum in yeast. *EMBO J.* 39:e102586. https://doi.org/10.15252/embj.2019102586

Schindelin, J., I. Arganda-Carreras, E. Frise, V. Kaynig, M. Longair, T. Pietzsch, S. Preibisch, C. Rueden, S. Saalfeld, B. Schmid, et al. 2012. Fiji: An open-source platform for biological-image analysis. *Nat. Methods.* 9: 676–682. https://doi.org/10.1038/nmeth.2019

Schuck, S., W.A. Prinz, K.S. Thorn, C. Voss, and P. Walter. 2009. Membrane expansion alleviates endoplasmic reticulum stress independently of the unfolded protein response. *J. Cell Biol.* 187:525–536. https://doi.org/10.1083/jcb.200907074

Schuck, S., C.M. Gallagher, and P. Walter. 2014. ER-phagy mediates selective degradation of endoplasmic reticulum independently of the core autophagy machinery. *J. Cell Sci.* 127:4078–4088. https://doi.org/10.1242/jcs.154716

Downloaded from http://rupress.org/jcb/article-pdf/223/11/e202307035/1931486/jcb_202307035.pdf by University Colorado Boulder user on 23 October 2024

Schuler, M.H., A.M. English, L. VanderMeer, J.M. Shaw, and A.L. Hughes. 2020. Amino acids promote mitochondrial-derived compartment formation in mammalian cells. *bioRxiv*. https://doi.org/10.1101/2020.12.23.424218 (Preprint posted December 23, 2020).

Schuler, M.H., A.M. English, T. Xiao, T.J. Campbell, J.M. Shaw, and A.L. Hughes. 2021. Mitochondrial-derived compartments facilitate cellular adaptation to amino acid stress. *Mol. Cell*. 81:3786–3802.e13. https://doi.org/10.1016/j.molcel.2021.08.021

Schweers, R.L., J. Zhang, M.S. Randall, M.R. Loyd, W. Li, F.C. Dorsey, M. Kundu, J.T. Opferman, J.L. Cleveland, J.L. Miller, et al. 2007. NIX is required for programmed mitochondrial clearance during reticulocyte maturation. *Proc. Natl. Acad. Sci. U S A*. 104:19500–19505. https://doi.org/10.1073/pnas.0708818104

Sheff, M.A., and K.S. Thorn. 2004. Optimized cassettes for fluorescent protein tagging in Saccharomyces cerevisiae. *Yeast*. 21:661–670. https://doi.org/10.1002/yea.1130

Shetty, A., N.I. Reim, and F. Winston. 2019. Auxin-inducible degron system for depletion of proteins in Saccharomyces cerevisiae. *Curr. Protoc. Mol. Biol.* 128:e104. https://doi.org/10.1002/cpmb.104

Sikorski, R.S., and P. Hieter. 1989. A system of shuttle vectors and yeast host strains designed for efficient manipulation of DNA in Saccharomyces cerevisiae. *Genetics*. 122:19–27. https://doi.org/10.1093/genetics/122.1.19

Soubannier, V., G.L. McLelland, R. Zunino, E. Braschi, P. Rippstein, E.A. Fon, and H.M. McBride. 2012a. A vesicular transport pathway shuttles cargo from mitochondria to lysosomes. *Curr. Biol.* 22:135–141. https://doi.org/10.1016/j.cub.2011.11.057

Soubannier, V., P. Rippstein, B.A. Kaufman, E.A. Shoubridge, and H.M. McBride. 2012b. Reconstitution of mitochondria derived vesicle formation demonstrates selective enrichment of oxidized cargo. *PLoS One*. 7:e52830. https://doi.org/10.1371/journal.pone.0052830

Stephan, T., C. Brüser, M. Deckers, A.M. Steyer, F. Balzarotti, M. Barbot, T.S. Behr, G. Heim, W. Hübner, P. Ilgen, et al. 2020. MICOS assembly controls mitochondrial inner membrane remodeling and crista junction redistribution to mediate cristae formation. *EMBO J.* 39:e104105. https://doi.org/10.15252/embj.2019104105

Sugiura, A., G.L. McLelland, E.A. Fon, and H.M. McBride. 2014. A new pathway for mitochondrial quality control: Mitochondrial-derived vesicles. *EMBO J.* 33:2142–2156. https://doi.org/10.15252/embj.201488104

Suzuki, K., M. Akioka, C. Kondo-Kakuta, H. Yamamoto, and Y. Ohsumi. 2013. Fine mapping of autophagy-related proteins during autophagosome formation in Saccharomyces cerevisiae. *J. Cell Sci.* 126:2534–2544. https://doi.org/10.1242/jcs.122960

Towers, C.G., D.K. Wodetzki, J. Thorburn, K.R. Smith, M.C. Caino, and A. Thorburn. 2021. Mitochondrial-derived vesicles compensate for loss of LC3-mediated mitophagy. *Dev. Cell*. 56:2029–2042.e5. https://doi.org/10.1016/j.devcel.2021.06.003

Weill, U., I. Yofe, E. Sass, B. Stynen, D. Davidi, J. Natarajan, R. Ben-Menachem, Z. Avihou, O. Goldman, N. Harpaz, et al. 2018. Genome-wide SWAp-Tag yeast libraries for proteome exploration. *Nat. Methods*. 15:617–622. https://doi.org/10.1038/s41592-018-0044-9

West, M., N. Zurek, A. Hoenger, and G.K. Voeltz. 2011. A 3D analysis of yeast ER structure reveals how ER domains are organized by membrane curvature. *J. Cell Biol.* 193:333–346. https://doi.org/10.1083/jcb.201011039

Wilson, Z.N., D. Buysse, M. West, D. Ahrens, and G. Odorizzi. 2021. Vacuolar H+-ATPase dysfunction rescues intralumenal vesicle cargo sorting in yeast lacking PI(3,5)P2 or Doa4. *J. Cell Sci.* 134:jcs258459. https://doi.org/10.1242/jcs.258459

Wilson, Z.N., S.S. Balasubramaniam, S. Wong, M.-H. Schuler, M.J. Wopat, and A.L. Hughes. 2024. Mitochondrial-derived compartments remove surplus proteins from the outer mitochondrial membrane. *J. Cell Biol.* 223. https://doi.org/10.1083/jcb.202307036

Wong, E.D., J.A. Wagner, S.W. Gorsich, J.M. McCaffery, J.M. Shaw, and J. Nunnari. 2000. The dynamin-related GTPase, Mgm1p, is an intermembrane space protein required for maintenance of fusion competent mitochondria. *J. Cell Biol.* 151:341–352. https://doi.org/10.1083/jcb.151.2.341

Wright, R., M. Basson, L. D'Ari, and J. Rine. 1988. Increased amounts of HMG-CoA reductase induce "karmellae": A proliferation of stacked membrane pairs surrounding the yeast nucleus. *J. Cell Biol.* 107:101–114. https://doi.org/10.1083/jcb.107.1.101

Xiao, T., A.M. English, Z.N. Wilson, J.A. Maschek, J.E. Cox, and A.L. Hughes. 2024. The phospholipids cardiolipin and phosphatidylethanolamine differentially regulate MDC biogenesis. *J. Cell Biol.* 223. https://doi.org/10.1083/jcb.202302069

Yamashita, A., M. Fujimoto, K. Katayama, S. Yamaoka, N. Tsutsumi, and S. Arimura. 2016. Formation of mitochondrial outer membrane derived protrusions and vesicles in Arabidopsis thaliana. *PLoS One*. 11:e0146717. https://doi.org/10.1371/journal.pone.0146717

Yao, P.J., E. Eren, R.S. Petralia, J.W. Gu, Y.X. Wang, and D. Kapogiannis. 2020. Mitochondrial protrusions in neuronal cells. *iScience*. 23:101514. https://doi.org/10.1016/j.isci.2020.101514

Youle, R.J., and A.M. van der Bliek. 2012. Mitochondrial fission, fusion, and stress. *Science*. 337:1062–1065. https://doi.org/10.1126/science.1219855

Zhen, Y., M. Radulovic, M. Vietri, and H. Stenmark. 2021. Sealing holes in cellular membranes. *EMBO J.* 40:e106922. https://doi.org/10.15252/embj.2020106922

Downloaded from http://rupress.org/jcb/article-pdf/223/11/e202307035/1931486/jcb_202307035.pdf by University Colorado Boulder user on 23 October 2024

Supplemental material

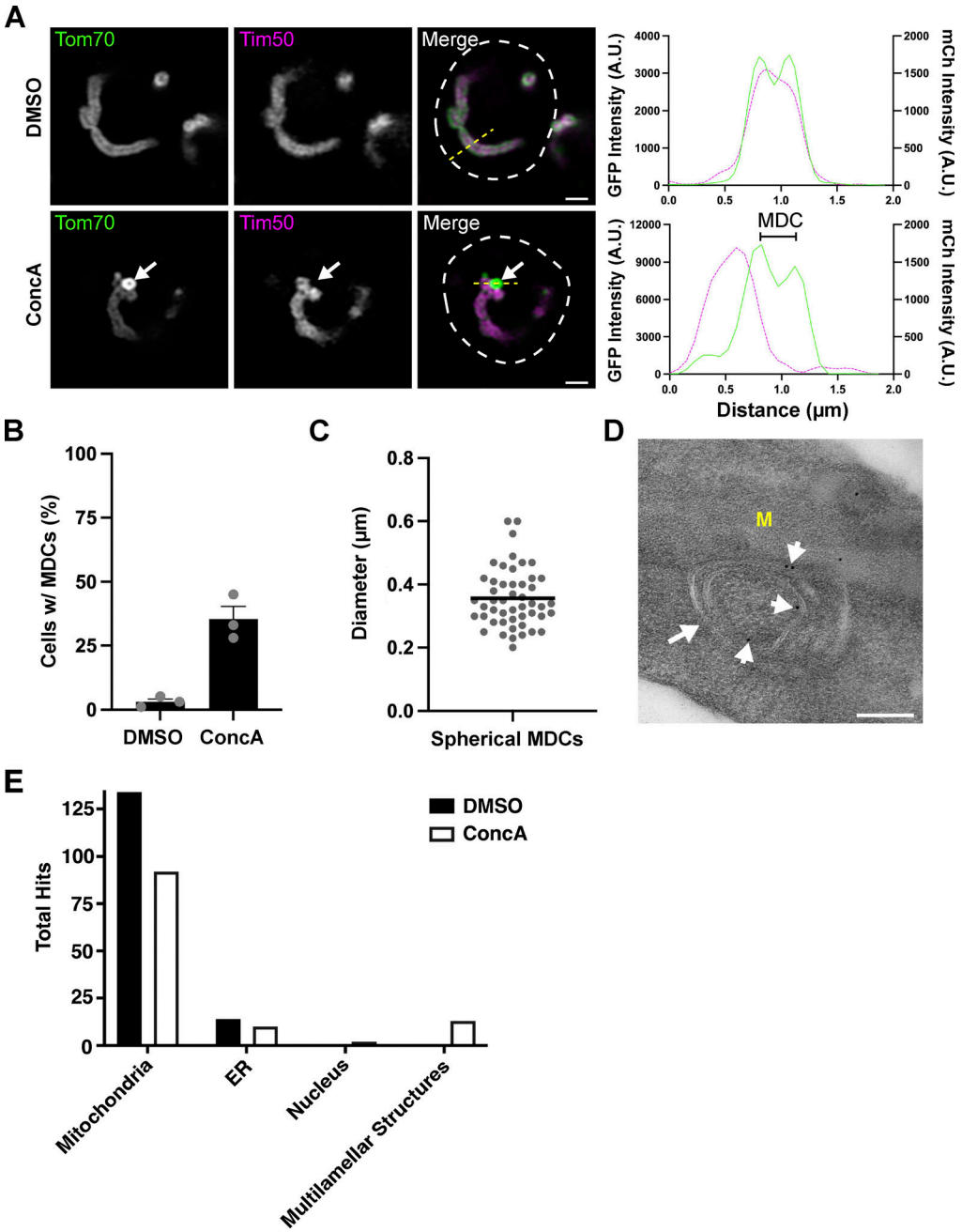

Figure S1. **ConcA-treated yeast also produce mitochondrial-derived multilamellar structures. (A)** Super-resolution confocal fluorescence microscopy images of haploid yeast expressing Tom70-yEGFP and Tim50-mCherry treated with either DMSO or 500 nM ConcA. MDCs are indicated by white arrows. Scale bar = 1 µm. The yellow line marks the position of the line-scan fluorescence intensity profile shown to the right. The left and right y axes correspond to Tom70-yEGFP and Tim50-mCherry fluorescence intensity, respectively. Bracket marks MDC. **(B)** Quantification of MDC formation in DMSO or ConcA-treated yeast. Error bars show mean ± SE of three replicates, $n \geq 100$ cells per replicate. **(C)** Scatter plot showing the diameter of ConcA-induced MDCs. The black line indicates the mean (0.36 µm) of $n = 49$ MDCs. **(D)** Thin-section TEM analysis of 80-nm cell sections from the same yeast strain analyzed above treated with 500 nM ConcA. Sections were stained with monoclonal antibodies targeting GFP and secondary antibodies conjugated to 10-nm gold particles. White arrow: multilamellar structures, white arrowheads point to gold particles, M: mitochondria. Scale bar = 200 nm. **(E)** Quantification of the total anti-GFP immunogold particles that labeled the indicated cell structures from an analysis of >100 cell sections from yeast expressing Tom70-yEGFP that were treated with either DMSO (vehicle) or 500 nM ConcA.

Downloaded from http://rupress.org/jcb/article-pdf/223/11/e202307035/1931486/jcb_202307035.pdf by University Colorado Boulder user on 23 October 2024

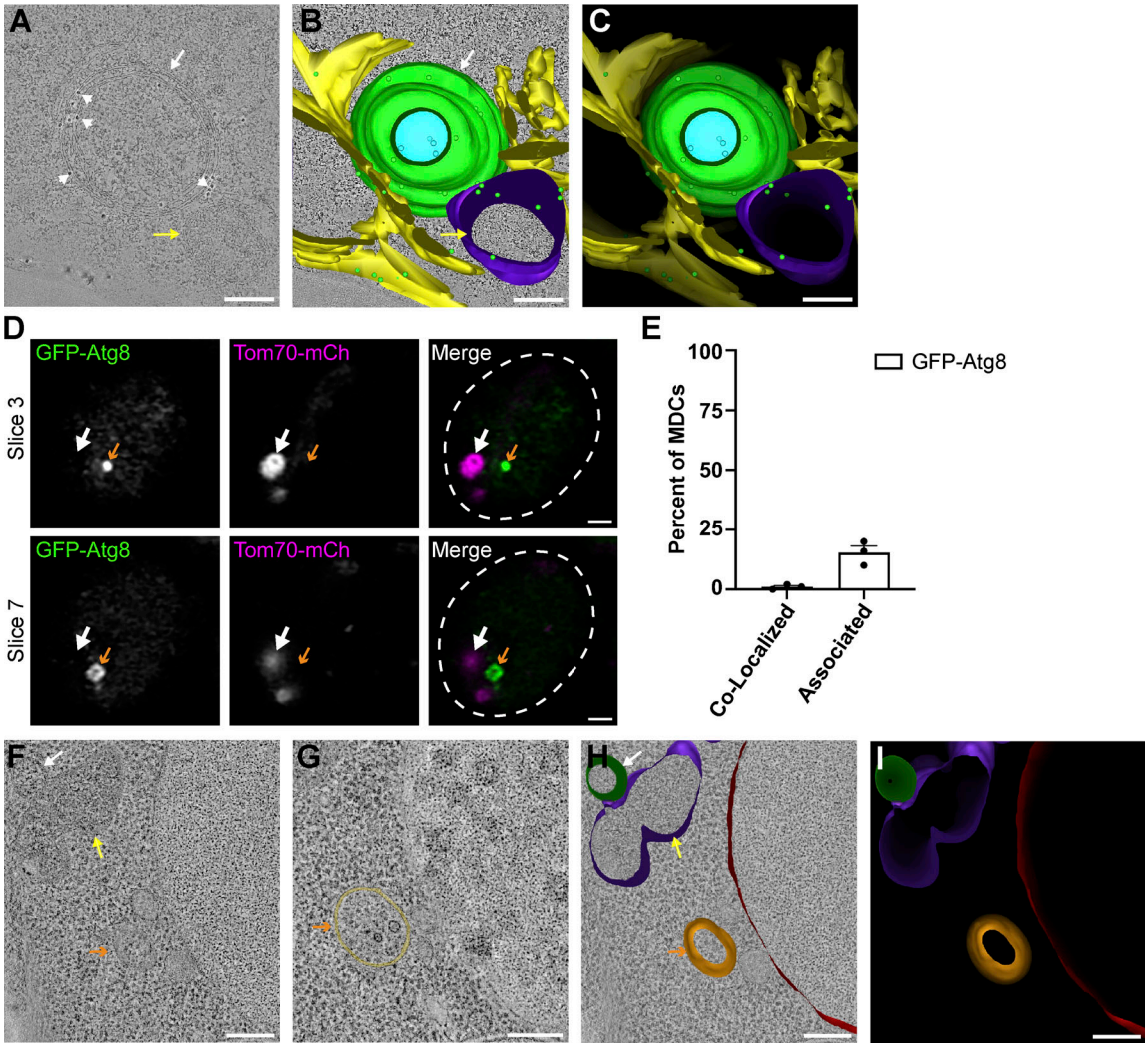

Figure S2. **MDCs are not bound by autophagosomal membranes. (A–C)** 2D cross sections and a 3D model derived from five serial 90-nm cell sections of the same yeast strain analyzed in Fig. 1. Sections were immunolabeled with antibodies targeting GFP and secondary antibodies conjugated to 10-nm gold particles. Scale bar = 200 nm. See associated Video 7. **(A)** Tomograph of a large, multilamellar structure strongly labeled with antibodies targeting Tom70-yEGFP. Yellow arrow: mitochondria, white arrow: multilamellar structure; white arrowheads point to gold particles. **(B)** Model overlay of the tomograph shown in A. **(C)** 3D model of a large, multilamellar structure bound by two closely apposed paired membranes. The limiting membrane of the outer doublet membrane is labeled green, while the internal doublet membrane is labeled cyan. Mitochondria: purple, ER: yellow; 10-nm gold particles are overlayed with green spheres. **(D)** Representative super-resolution confocal fluorescence microscopy images of yeast expressing Tom70-mCherry and sfGFP-Atg8 after a 2-h treatment with 200 nM Rap. White arrow marks MDC, orange arrow marks sfGFP-Atg8–positive structures. The images shown are from the same cell but show different z-slices, which are labeled. Scale bar = 1 µm. **(E)** Quantification of the frequency sfGFP-Atg8 foci were colocalized or closely associated with Tom70-mCherry–marked MDCs. Error bars show mean ± SE of three replicates, $n \geq 100$ MDCs per replicate. **(F–I)** 2D cross sections and 3D models from different views of the same tomogram shown in Fig. 3, A–C. Scale bars = 200 nm. **(F and G)** Two different 2D cross sections from a larger view of the same tomogram are shown in Fig. 3, A–C. White arrow: MDC, yellow arrow: mitochondria, orange arrow: autophagosome. **(H)** Model overlay of the tomograph shown in F. **(I)** 3D model of a vacuole-associated autophagosome labeled in orange, MDC labeled in green, mitochondria labeled in purple, and the vacuole labeled in red.

Downloaded from http://rupress.org/jcb/article-pdf/223/11/e202307035/1931486/jcb_202307035.pdf by University Colorado Boulder user on 23 October 2024

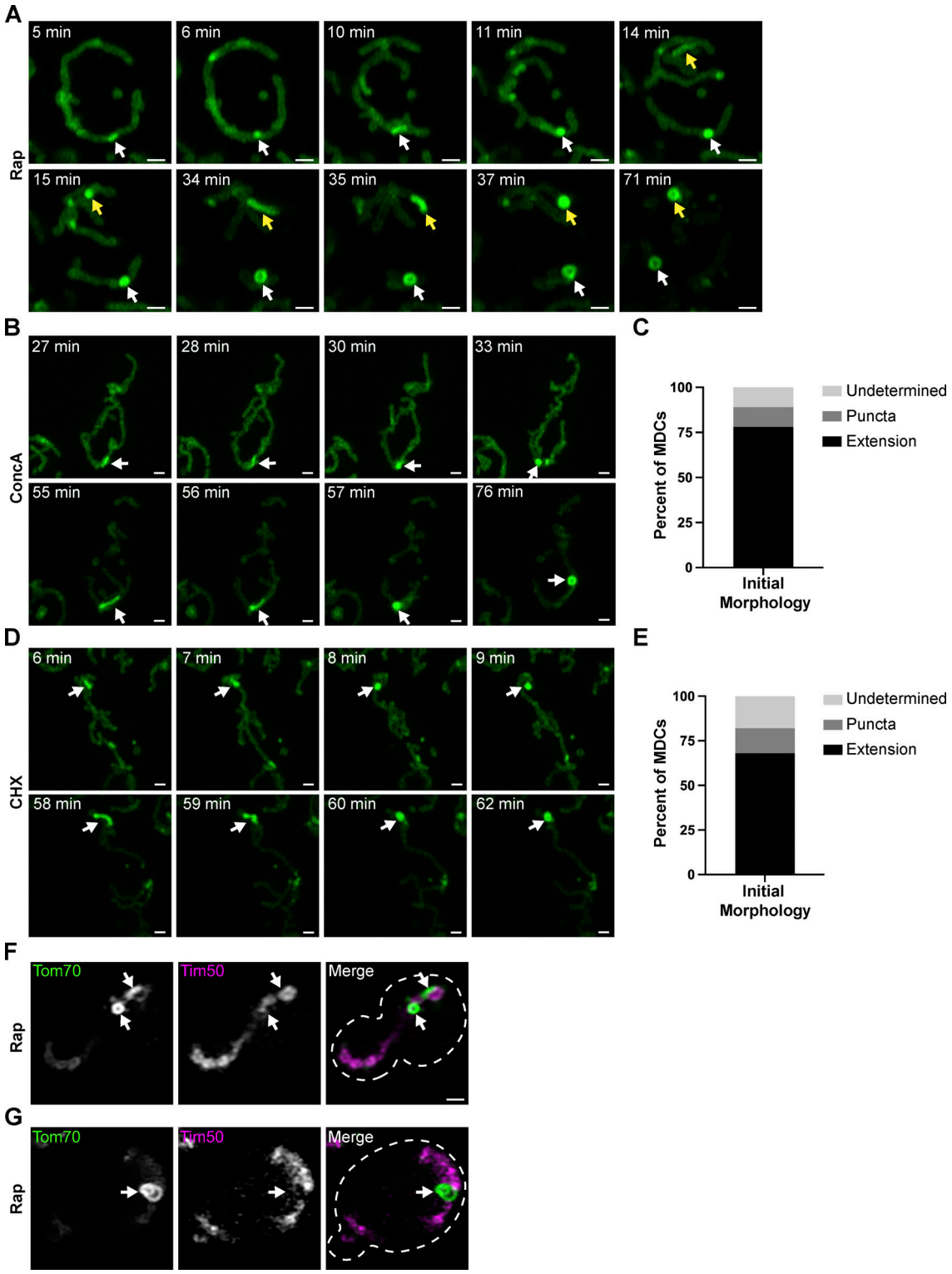

Figure S3. **MDCs form through membrane extension intermediates. (A)** Super-resolution time-lapse images of Rap-induced MDC formation in yeast cells expressing Tom70-yEGFP. Images were acquired over 120 min. White and yellow arrows mark two different MDCs. Scale bar = 1 µm. See associated Video 8. **(B)** Super-resolution time-lapse images of ConcA-induced MDC formation in yeast cells expressing Tom70-yEGFP. Images were acquired over 120 min. White arrows mark MDCs. Scale bar = 1 µm. See associated Video 9. **(C)** Quantification of the initial morphology of Tom70-yEGFP structures during MDC biogenesis after ConcA treatment. *n* = 59 events from three experiments. **(D)** Super-resolution time-lapse images of CHX-induced MDC formation in yeast cells expressing Tom70-yEGFP. Images were acquired over 120 min. White arrows mark MDCs. Scale bar = 1 µm. See associated Video 10. **(E)** Quantification of the initial morphology of Tom70-yEGFP structures during MDC biogenesis after CHX treatment. *n* = 54 events from three experiments. **(F)** Representative super-resolution confocal fluorescence microscopy image of a cell with two MDCs with different morphologies. MDCs are marked by white arrows. **(G)** Representative super-resolution confocal fluorescence microscopy image of an MDC with resolvable layers of Tom70-yEGFP. MDC is marked by the white arrow.

Downloaded from http://rupress.org/jcb/article-pdf/223/11/e202307035/1931486/jcb_202307035.pdf by University Colorado Boulder user on 23 October 2024

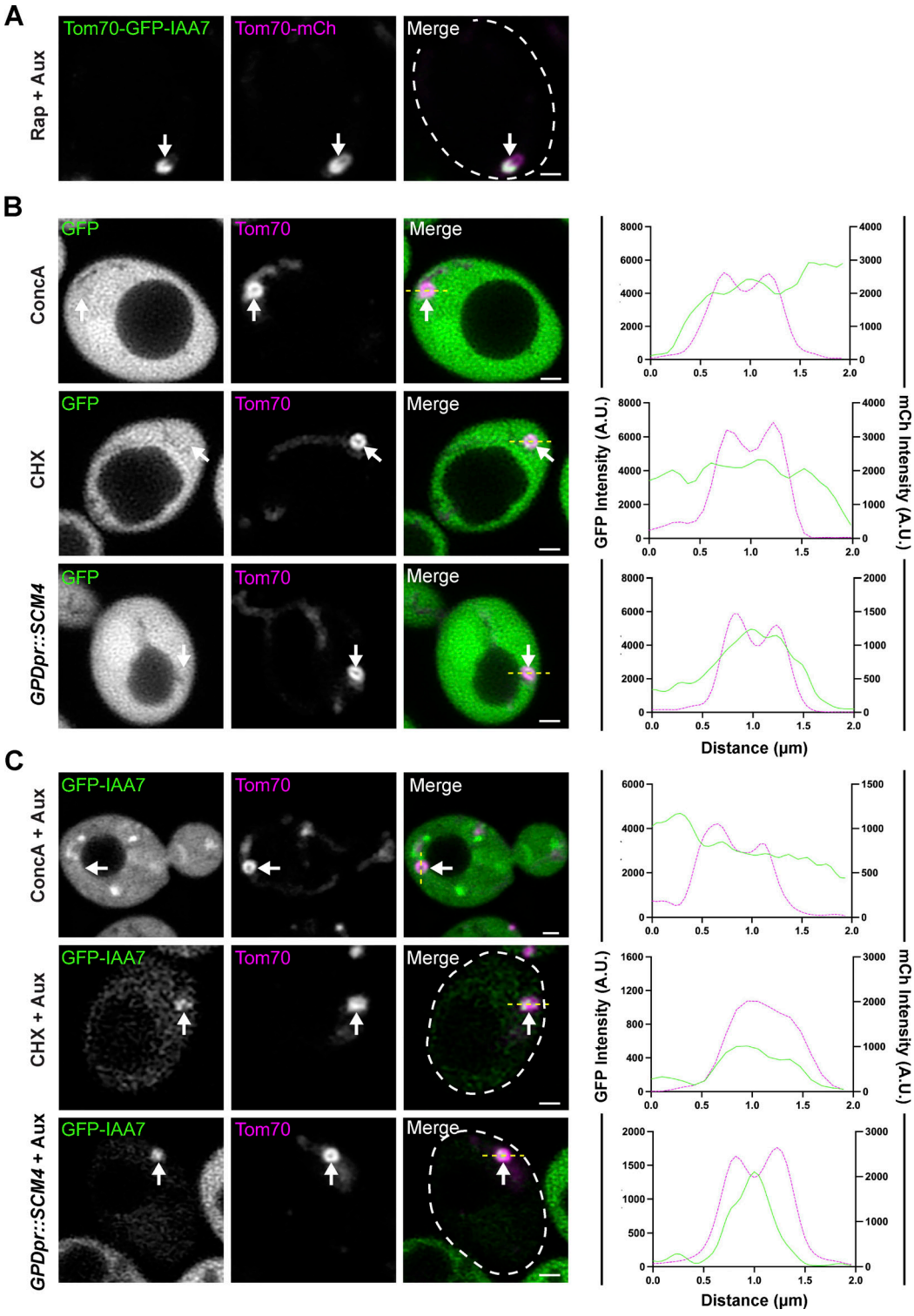

Figure S4. **The MDC lumen contains cytosolic material. (A)** Super-resolution confocal fluorescence microscopy images of yeast cells expressing Tom70-GFP-IAA7 and Tom70-mCherry. Images were taken 2 h after treatment with 1 mM auxin, which was added after a 2-h pretreatment with Rap (Rap + Aux). MDCs are indicated by white arrows. Scale bar = 1 µm. **(B)** Super-resolution confocal fluorescence microscopy images of MDC formation in yeast expressing yEGFP and Tom70-mCherry. MDCs were induced with either ConcA, CHX, or overexpression of the OMM protein Scm4 (*GPDpr::SCM4*). MDCs are indicated by white arrows. Scale Bar = 1 µm. The yellow line marks the position of the line-scan fluorescence intensity profile shown to the right. The left and right y axes correspond to yEGFP and Tom70-mCherry fluorescence intensity, respectively. **(C)** Representative super-resolution confocal fluorescence microscopy images of yeast expressing yEGFP-IAA7 and Tom70-mCherry. After a 2-h treatment with ConcA or CHX, cells were subsequently treated with 1 mM auxin (ConcA + Aux and CHX + Aux). Cells overexpressing the OMM protein Scm4 (*GPDpr::SCM4*) were treated with 1 mM auxin (*GPDpr::SCM4* + Aux). White arrows mark MDCs. Scale bar = 1 µm. The yellow line denotes the position of the line-scan fluorescence intensity profile shown to the right. The left and right y axes correspond to GFP and Tom70-mCherry fluorescence intensity, respectively.

Downloaded from http://rupress.org/jcb/article-pdf/223/11/e202307035/1931486/jcb_202307035.pdf by University Colorado Boulder user on 23 October 2024

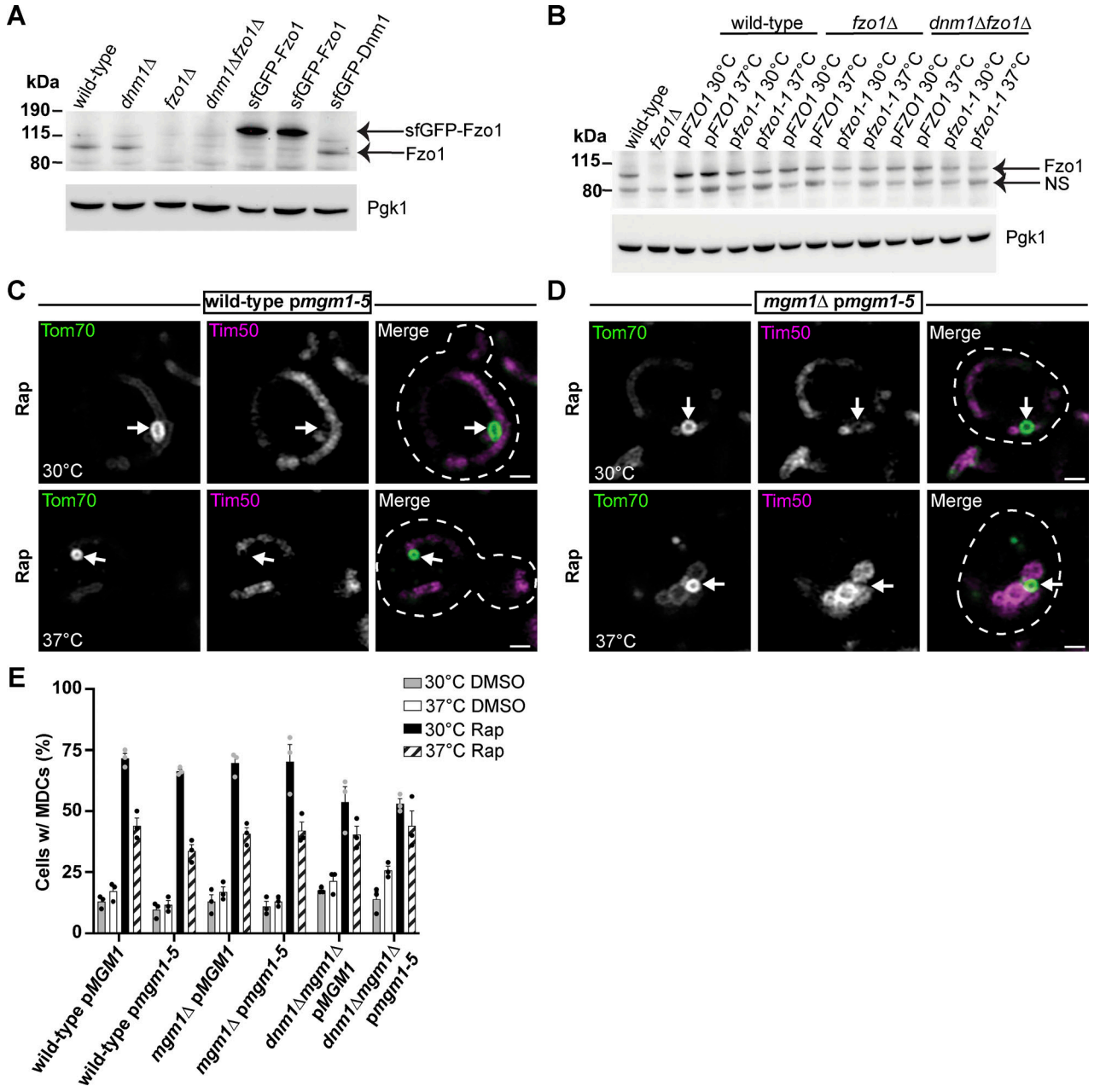

Figure S5. **The mitochondrial fission and fusion machinery perform competing roles in MDC formation. (A)** Immunoblots of whole-cell protein extracts from the indicated yeast strains probed for Fzo1 using an antibody that targets the N-terminus of Fzo1. Arrows point to protein bands for sfGFP-Fzo1 and Fzo1. Note that sfGFP-Fzo1 is expressed from the *NOP1* promoter. Pgk1 is shown as a loading control. **(B)** Immunoblots of whole-cell protein extracts from the indicated yeast strains at the indicated temperatures, all probed for Fzo1 using an antibody that targets the N-terminus of Fzo1. Arrows point to protein bands for Fzo1 and a non-specific (NS) protein. Pgk1 is shown as a loading control. **(C and D)** Super-resolution confocal fluorescence microscopy images of wild-type (C) or *mgm1*Δ (D) yeast cells expressing *mgm1-5*, Tom70-yEGFP, and Tim50-mCherry treated with 200 nM Rap at the indicated temperatures. MDCs are indicated by white arrows. Scale bar = 1 µm. **(E)** Quantification of MDC formation in the indicated yeast strains upon treatment with either DMSO or Rap at the indicated temperatures. Error bars show mean ± SE of three replicates, $n \geq 100$ cells per replicate. Source data are available for this figure: SourceData FS5.

Video 1. **Related to** Fig. 2**.** Mitochondrial-derived multilamellar structures are enriched for Tom70-GFP and exclude Tim50-mCherry. Z-series and 3D model of the tomogram shown in Fig. 2. The video is compiled at 50 frames per second. Scale bar = 200 nm.

Downloaded from http://rupress.org/jcb/article-pdf/223/11/e202307035/1931486/jcb_202307035.pdf by University Colorado Boulder user on 23 October 2024

Video 2. **Related to** Fig. 3, A–C**.** Mitochondrial-derived compartments contain sets of paired membranes. Z-series and 3D model of the tomogram shown in Fig. 3, A–C. The video is compiled at 50 frames per second. Scale bar = 200 nm.

Video 3. **Related to** Fig. 3, D–F**.** Mitochondrial-derived compartments contain sets of paired membranes. Z-series and 3D model of the tomogram shown in Fig. 3, D–F. The video is compiled at 50 frames per second. Scale bar = 200 nm.

Video 4. **Related to** Fig. 3, G–I**.** Mitochondrial-derived compartments contain sets of paired membranes. Z-series and 3D model of the tomogram shown in Fig. 3, G–I. The video is compiled at 50 frames per second. Scale bar = 200 nm.

Video 5. **Related to** Fig. 4 A**.** Mitochondrial-derived compartments form through membrane extension intermediates. Maximum intensity projections of yeast expressing Tom70-yEGFP and Tim50-mCherry treated with Rap. Images were taken every minute (min) and are shown at four frames per second. Scale bar = 1 µm.

Video 6. **Related to** Fig. 4 C**.** Mitochondrial-derived compartments form through membrane extension intermediates. Maximum intensity projections of yeast expressing Tom70-yEGFP treated with Rap. Images were taken every minute (min) and are shown at four frames per second. Scale bar = 1 µm.

Video 7. **Related to** Fig. S2**.** Mitochondrial-derived compartments contain sets of paired membranes. Z-series and 3D model of the tomogram shown in Fig. S2, A–C. The video is compiled at 50 frames per second. Scale bar = 200 nm.

Video 8. **Related to** Fig. S3 A**.** Mitochondrial-derived compartments form through membrane extension intermediates. Maximum intensity projections of yeast expressing Tom70-yEGFP treated with Rap. Images were taken every minute (min) and are shown at four frames per second. Scale bar = 1 µm.

Video 9. **Related to** Fig. S3 B**.** Mitochondrial-derived compartments form through membrane extension intermediates. Maximum intensity projections of yeast expressing Tom70-yEGFP treated with ConcA. Images were taken every minute (min) and are shown at four frames per second. Scale bar = 1 µm.

Video 10. **Related to** Fig. S3 D**.** Mitochondrial-derived compartments form through membrane extension intermediates. Maximum intensity projections of yeast expressing Tom70-yEGFP treated with CHX. Images were taken every minute (min) and are shown at four frames per second. Scale bar = 1 µm.

Provided online are three tables. Table S1 lists the yeast strains used in this study. Table S2 lists the oligonucleotides used in this study. Table S3 lists bacterial strains, chemicals, plasmids, and software used in this study.

Downloaded from http://rupress.org/jcb/article-pdf/223/11/e202307035/1931486/jcb_202307035.pdf by University Colorado Boulder user on 23 October 2024